The XXL Survey: First results

The XXL Survey[*],[**]

III. Luminosity-temperature relation of the bright cluster sample

P. A. Giles[1], B. J. Maughan[1], F. Pacaud[2], M. Lieu[3], N. Clerc[4], M. Pierre[5], C. Adami[6], L. Chiappetti[7], J. Démoclés[3], S. Ettori[8,9], J. P. Le Févre[5], T. Ponman[3], T. Sadibekova[6], G. P. Smith[3], J. P. Willis[10], and F. Ziparo[3]

[1] School of Physics, HH Wills Physics Laboratory, Tyndall Avenue, Bristol, BS8 1TL, UK
e-mail: P.Giles@bristol.ac.uk
[2] Argelander-Institut fur Astronomie, University of Bonn, Auf dem Hügel 71, 53121 Bonn, Germany
[3] School of Physics and Astronomy, University of Birmingham, Edgbaston, Birmingham, B15 2TT, UK
[4] Max-Planck Institut fur Extraterrestrische Physik, Postfach 1312, 85741 Garching bei Munchen, Germany
[5] Laboratoire AIM, CEA/DSM/IRFU/Sap, CEA Saclay, 91191 Gif-sur-Yvette, France
[6] LAM (Laboratoire d'Astrophysique de Marseille) UMR 7326, Aix-Marseille Université, CNRS, 13388 Marseille, France
[7] INAF, IASF Milano, via Bassini 15, 20133 Milano, Italy
[8] INAF, Osservatorio Astronomico di Bologna, via Ranzani 1, 40127 Bologna, Italy
[9] INFN, Sezione di Bologna, viale Berti Pichat 612, 40127 Bologna, Italy
[10] Department of Physics and Astronomy, University of Victoria, 3800 Finnerty Road, Victoria, BC, Canada

ABSTRACT

Context. The XXL Survey is the largest homogeneous survey carried out with *XMM-Newton*. Covering an area of 50 deg^2, the survey contains several hundred galaxy clusters out to a redshift of ~2 above an X-ray flux limit of ~5×10^{-15} erg cm^{-2} s^{-1}. This paper belongs to the first series of XXL papers focusing on the bright cluster sample.
Aims. We investigate the luminosity-temperature (LT) relation for the brightest clusters detected in the XXL Survey, taking fully into account the selection biases. We investigate the form of the LT relation, placing constraints on its evolution.
Methods. We have classified the 100 brightest clusters in the XXL Survey based on their measured X-ray flux. These 100 clusters have been analysed to determine their luminosity and temperature to evaluate the LT relation. We used three methods to fit the form of the LT relation, with two of these methods providing a prescription to fully take into account the selection effects of the survey. We measure the evolution of the LT relation internally using the broad redshift range of the sample.
Results. Taking fully into account selection effects, we find a slope of the bolometric LT relation of $B_{LT} = 3.08 \pm 0.15$, steeper than the self-similar expectation ($B_{LT} = 2$). Our best-fit result for the evolution factor is $E(z)^{1.64 \pm 0.77}$, fully consistent with "strong self-similar" evolution where clusters scale self-similarly with both mass and redshift. However, this result is marginally stronger than "weak self-similar" evolution, where clusters scale with redshift alone. We investigate the sensitivity of our results to the assumptions made in our fitting model, finding that using an external LT relation as a low-z baseline can have a profound effect on the measured evolution. However, more clusters are needed in order to break the degeneracy between the choice of likelihood model and mass-temperature relation on the derived evolution.

Key words. X-rays: galaxies: clusters – galaxies: clusters: general – galaxies: clusters: intracluster medium

1. Introduction

Under the assumption of self-similarity (Kaiser 1986), simple scaling laws can be derived between various properties of galaxy clusters. These scaling laws are advantageous as they provide a cheap way of measuring the masses of large samples of clusters, an important ingredient for cosmological studies using galaxy clusters (see Allen et al. 2011, for a review). One of the most explored scaling relations is that between the X-ray luminosity (L) and temperature (T), expected to follow a relationship of $L \propto T^2$. However, a multitude of studies have found that the slope of the LT relation is ~3 (e.g. Pratt et al. 2009;

Eckmiller et al. 2011; Takey et al. 2013; Connor et al. 2014), steeper than the self-similar expectation. One of the main explanations for the deviation from this theoretical expectation is energy input by non-gravitational processes during cluster formation at early times, including pre-heating, supernovae feedback, and heating from active galactic nuclei (AGN) at high redshift. These non-gravitational processes should have the strongest effect in lower mass systems owing to their shallower potential wells that expel gas from the inner regions and suppress the luminosity. Observations have shown further steepening of the LT relation at the low-mass regime (e.g. Osmond & Ponman 2004; Sun et al. 2009). However, recent work, using methods to correct for sample selection effects, has suggested that the slope of the LT relation on group scales is consistent with massive clusters (e.g. Bharadwaj et al. 2015; Lovisari et al. 2015).

X-ray flux limited samples suffer from two forms of selection bias, Malmquist bias, where higher luminosity clusters are preferentially selected out to higher redshifts, and Eddington bias,

---

where in the presence of intrinsic or statistical scatter in luminosity for a given mass, objects above a flux limit will have above average luminosities for their mass. This effect is amplified by the steep slope of the cluster mass function, which results in a net movement of lower mass objects into a flux limited sample. The net effect on the LT relation is to bias the normalisation high and the slope low (see Allen et al. 2011, for a review). Therefore, taking these biases into account is paramount when modelling cluster scaling relations in order to uncover the true nature of any non-gravitational heating driving departures from self-similar behaviour with mass or redshift. Although scaling relation studies have had a rich history, only a relatively small number of published relations attempt to account for selection biases (e.g. Stanek et al. 2006; Pacaud et al. 2007; Pratt et al. 2009; Vikhlinin et al. 2009; Andreon & Bergé 2012; Bharadwaj et al. 2015; Lovisari et al. 2015), while Mantz et al. (2010a) provides the most robust handling of selection effects to date.

In the self-similar model, with cluster properties measured within overdensity radii defined relative to the critical density, the evolution of the scaling relations can be parameterised by the factor $E(z)$ (where $E(z) = \sqrt{\Omega_M(1+z)^3 + (1 - \Omega_M - \Omega_\Lambda)(1+z)^2 + \Omega_\Lambda}$). In this framework, the evolution of the normalisation of the LT relation goes as $E(z)^{\gamma_{LT}}$, where $\gamma_{LT} \equiv 1$ if clusters scale self-similarly with both mass and redshift, or $\gamma_{LT} \approx 0.42$ if the observed mass dependence of the cluster baryon fraction is also included (Maughan 2014). These two reference values for γ_{LT} assume the same underlying evolution driven by the changing critical density of the Universe; the difference arises purely from the algebraic combination of the scaling laws of gas mass, temperature, and gas structure with total mass that are used to construct the LT relation (Maughan 2014).

We refer to $\gamma_{LT} = 1$ as strong self-similar evolution, reflecting the fact that it is based on the assumption that clusters scale self-similarly with both mass and redshift, while $\gamma_{LT} = 0.42$ is referred to as weak self-similar evolution and assumes clusters only scale self-similarly with redshift. The latter is a more realistic prediction of the self-similar evolution against which to test for departures in the observed evolution of clusters in the LT plane.

Understanding how scaling relations evolve with redshift is important for two main reasons: (i) scaling relations must be well-calibrated at high redshift to provide mass estimates for cosmology and (ii) the relations provide insight into the history of heating mechanisms in clusters. A consensus on the evolution from observations has yet to be achieved; various studies find an evolution consistent with self-similar (e.g. Vikhlinin et al. 2002; Maughan et al. 2006; Pacaud et al. 2007), while others find departures from the self-similar expectation (e.g. Ettori et al. 2004; Kotov & Vikhlinin 2005; Reichert et al. 2011; Hilton et al. 2012; Clerc et al. 2014). Again, the importance of taking into account selection effects is crucial for understanding evolution and recent work has shown that departures from self-similar evolution can be explained by selection biases (Pacaud et al. 2007; Mantz et al. 2010a; Maughan et al. 2012). Although these processes need to be understood to explain the differences between the observed and theoretical prediction, further considerations must be made to take into account the selection effects.

In order to address the points raised above, we have carried out the largest X-ray survey undertaken by *XMM-Newton*. The XXL Survey (Pierre et al. 2016, hereafter Paper I), is a 50 deg^2 survey with an X-ray sensitivity of $\sim 5 \times 10^{-15}$ erg s^{-1} cm^{-2} (for point-like sources), in the [0.5–2] keV band. With the aim of

detecting several hundred clusters out to a redshift of ≈ 2, this survey provides a unique opportunity to constrain cluster scaling relations that fully accounts for selection effects, and in the future will place robust constraints on cosmological parameters (see Paper I).

In this paper, part of the first release of XXL results, we investigate the form of the luminosity-temperature relation (LT) for a sample of the 100 brightest clusters detected in the XXL Survey. The LT relation will be derived taking the selection function of the cluster sample fully into account. The outline of this paper is as follows. In Sect. 2 we discuss the data preparation and sample selection. Section 3 outlines the cluster analysis. In Sect. 4 we present our results and derive the sample and bias-corrected scaling relations. Our discussion and conclusions are presented in Sects. 5 and 6, respectively. Throughout this paper we assume a WMAP9 cosmology of $H_0 = 70$ km/s/Mpc, $\Omega_\Lambda = 0.72$, and $\Omega_m = 0.28$ (Hinshaw et al. 2013).

2. Data processing and sample selection

The data processing and sample selection are fully detailed in Pacaud et al. (2016, hereafter Paper II), and is briefly summarised here. The XXL Survey contains 542 XMM pointings covering 50.8 deg^2. After light-curve filtering (following Pratt & Arnaud 2002), rejection of bad pointings and exclusion of pointings with high background levels, the total XXL area spans 46.6 deg^2 (from 454 pointings). Images, exposure maps, and detector masks were generated and processed using the XAMIN pipeline (Pacaud et al. 2006; Clerc et al. 2012). SEXTRACTOR was then run to generate a conservative source catalogue and source masks, followed by a dedicated XMM maximum likelihood fitting procedure to determine likelihood ratios to assess the detection and source extent probabilities. Extended sources were defined with an extent larger than 5″ and extension likelihood larger than 15. These extended sources were then separated into two classes, the C1 class with extension likelihood larger than 33 and detection likelihood larger than 32, and the C2 class with an extension likelihood 15 < EXT_LH < 32.

The sample used in this work is the 100 brightest clusters (hereafter XXL-100-GC[1]) selected from the source list generated above. Count rates were estimated from a growth curve analysis (GCA, following Clerc et al. 2012) within a 60″ aperture, and converted into fluxes using an energy conversion factor (assuming $T = 3$ keV, $z = 0.3$, and $Z = 0.3$) of 9.04×10^{-13}, or 1.11×10^{-13} for clusters falling on the damaged mos1 chip. The clusters were ranked in order of decreasing flux and the brightest 100 clusters were selected. We note that five clusters within the XXL-100-GC fell on observations with high periods of flaring. The five flared observations were not used and instead the next five brightest objects were included. The clusters XLSSC 113, 114, 115, 550, and 551 were replaced with XLSSC 091, 506, 516, 545, and 548. Taking this into account, our selection corresponds to a flux limit of $F_{X,cut} = 3 \times 10^{-14}$ ergs s^{-1} cm^{-2}. The final XXL-100-GC sample consists of 96 C1 and 4 C2 clusters, respectively, with 51 falling within the northern field of the XXL footprint, and 49 within the southern field. Following a robust redshift validation (see Paper I), the XXL-100-GC span a redshift range of $0.04 \leq z \leq 1.05$, with 98 spectroscopic and 2 photometric redshifts. The sample and the derived properties can be found in Table 1.

---

[1] A master XXL-100-GC cluster catalogue will also be available in electronic form at http://cosmosdb.isaf-milano.inaf.it/XXL/ and via the XMM XXL DataBase at http://xmm-lss.in2p3.fr

Table 1. X-ray properties of the XXL-100-GC. $r_{500,\mathrm{MT}}$ is estimated from the $M_{\mathrm{WL}} - T$ relation in Sect. 3.

XLSSC Num	z	$E(z)$	$r_{500,\mathrm{MT}}$ Mpc	$T_{300\,\mathrm{kpc}}$ (keV)	$L_{300\,\mathrm{kpc}}^{\mathrm{XXL}}$ $10^{43}\,(\mathrm{erg\,s^{-1}})$	$L_{500,\mathrm{MT}}^{\mathrm{XXL}}$ $10^{43}\,(\mathrm{erg\,s^{-1}})$	$L_{500,\mathrm{MT}}^{\mathrm{bol}}$ $10^{43}\,(\mathrm{erg\,s^{-1}})$
XLSSC 001	0.614	1.38	0.777	$3.8^{+0.5}_{-0.4}$	7.56 ± 0.54	10.10 ± 0.72	23.48 ± 1.68
XLSSC 003	0.836	1.57	0.643	$3.4^{+1.0}_{-0.6}$	10.04 ± 1.21	12.32 ± 1.49	26.64 ± 3.22
XLSSC 006	0.429	1.24	0.982	$4.8^{+0.5}_{-0.4}$	11.44 ± 0.55	17.42 ± 0.83	46.72 ± 2.24
XLSSC 010	0.330	1.18	0.751	$2.7^{+0.5}_{-0.3}$	1.97 ± 0.16	2.58 ± 0.21	5.58 ± 0.46
XLSSC 011	0.054	1.02	0.831	$2.5^{+0.5}_{-0.4}$	0.11 ± 0.01	0.15 ± 0.01	0.33 ± 0.02
XLSSC 022	0.293	1.15	0.671	$2.1^{+0.1}_{-0.1}$	2.45 ± 0.09	3.06 ± 0.11	6.06 ± 0.22
XLSSC 023	0.328	1.17	0.655	$2.1^{+0.3}_{-0.2}$	1.32 ± 0.14	1.63 ± 0.18	3.21 ± 0.35
XLSSC 025	0.265	1.14	0.751	$2.5^{+0.2}_{-0.2}$	1.68 ± 0.08	2.21 ± 0.11	4.69 ± 0.23
XLSSC 027	0.295	1.15	0.768	$2.7^{+0.4}_{-0.3}$	1.11 ± 0.09	1.48 ± 0.11	3.20 ± 0.25
XLSSC 029	1.050	1.77	0.626	$4.1^{+1.0}_{-0.6}$	16.03 ± 1.38	19.46 ± 1.68	43.67 ± 3.76
XLSSC 036	0.492	1.29	0.801	$3.6^{+0.5}_{-0.4}$	8.21 ± 0.53	11.14 ± 0.72	25.78 ± 1.68
XLSSC 041	0.142	1.07	0.670	$1.9^{+0.1}_{-0.2}$	0.96 ± 0.06	1.19 ± 0.07	2.31 ± 0.14
XLSSC 050	0.140	1.07	0.897	$3.1^{+0.2}_{-0.2}$	1.93 ± 0.05	2.78 ± 0.07	6.68 ± 0.17
XLSSC 052	0.056	1.02	0.387	$0.6^{+0.0}_{-0.0}$	0.09 ± 0.01	0.09 ± 0.01	0.14 ± 0.01
XLSSC 054	0.054	1.02	0.723	$2.0^{+0.2}_{-0.2}$	0.21 ± 0.02	0.28 ± 0.02	0.56 ± 0.04
XLSSC 055	0.232	1.12	0.843	$3.0^{+0.3}_{-0.4}$	1.88 ± 0.11	2.61 ± 0.15	6.02 ± 0.34
XLSSC 056	0.348	1.19	0.824	$3.2^{+0.5}_{-0.3}$	3.03 ± 0.18	4.16 ± 0.25	9.58 ± 0.58
XLSSC 057	0.153	1.07	0.734	$2.2^{+0.3}_{-0.1}$	0.91 ± 0.05	1.18 ± 0.07	2.46 ± 0.14
XLSSC 060	0.139	1.07	1.136	$4.8^{+0.2}_{-0.2}$	3.75 ± 0.05	6.31 ± 0.08	18.57 ± 0.24
XLSSC 061	0.259	1.13	0.678	$2.1^{+0.5}_{-0.3}$	0.87 ± 0.11	1.09 ± 0.14	2.16 ± 0.27
XLSSC 062	0.059	1.03	0.422	$0.7^{+0.1}_{-0.1}$	0.10 ± 0.02	0.11 ± 0.02	0.16 ± 0.02
XLSSC 072	1.002	1.73	0.613	$3.7^{+1.1}_{-0.6}$	12.35 ± 1.49	14.89 ± 1.79	32.61 ± 3.92
XLSSC 083	0.430	1.24	0.943	$4.5^{+1.1}_{-0.7}$	3.14 ± 0.25	4.67 ± 0.38	12.11 ± 0.98
XLSSC 084	0.430	1.24	0.945	$4.5^{+1.6}_{-1.3}$	1.38 ± 0.21	2.04 ± 0.31	6.18 ± 0.84
XLSSC 085	0.428	1.24	0.976	$4.8^{+2.0}_{-1.0}$	2.56 ± 0.26	3.88 ± 0.40	11.46 ± 1.18
XLSSC 087	0.141	1.07	0.619	$1.6^{+0.1}_{-0.1}$	0.76 ± 0.07	0.92 ± 0.09	1.67 ± 0.16
XLSSC 088	0.295	1.15	0.726	$2.5^{+0.6}_{-0.4}$	1.22 ± 0.11	1.57 ± 0.15	3.28 ± 0.31
XLSSC 089	0.609	1.38	0.769	$3.7^{+1.6}_{-1.2}$	4.85 ± 0.66	6.44 ± 0.87	14.84 ± 2.01
XLSSC 090	0.141	1.07	0.507	$1.1^{+0.1}_{-0.1}$	0.38 ± 0.05	0.43 ± 0.05	0.67 ± 0.08
XLSSC 091	0.186	1.09	1.149	$5.1^{+0.2}_{-0.2}$	7.73 ± 0.11	13.12 ± 0.19	39.12 ± 0.58
XLSSC 092	0.432	1.24	0.771	$3.1^{+0.8}_{-0.6}$	2.11 ± 0.24	2.81 ± 0.31	6.24 ± 0.70
XLSSC 093	0.429	1.24	0.810	$3.4^{+0.6}_{-0.4}$	4.75 ± 0.31	6.47 ± 0.42	14.91 ± 0.96
XLSSC 094	0.886	1.62	0.742	$4.7^{+1.3}_{-0.9}$	19.85 ± 1.71	25.93 ± 2.24	62.01 ± 5.35
XLSSC 095	0.138	1.06	0.450	$0.9^{+0.1}_{-0.1}$	0.15 ± 0.03	0.17 ± 0.03	0.24 ± 0.04
XLSSC 096	0.520	1.31	1.000	$5.5^{+2.0}_{-1.1}$	3.77 ± 0.40	5.80 ± 0.62	16.05 ± 1.71
XLSSC 097	0.760	1.50	0.794	$4.6^{+1.5}_{-1.0}$	9.91 ± 1.25	13.37 ± 1.69	32.53 ± 4.11
XLSSC 098	0.297	1.15	0.801	$2.9^{+1.0}_{-0.6}$	1.28 ± 0.16	1.74 ± 0.21	3.88 ± 0.48
XLSSC 099	0.391	1.22	1.032	$5.1^{+3.1}_{-1.5}$	1.44 ± 0.26	2.26 ± 0.41	6.31 ± 1.13
XLSSC 100	0.915	1.64	0.694	$4.3^{+1.7}_{-1.2}$	11.12 ± 2.50	14.06 ± 3.17	32.42 ± 7.28
XLSSC 101	0.756	1.50	0.788	$4.6^{+0.8}_{-0.8}$	12.27 ± 0.96	16.53 ± 1.29	39.95 ± 3.13
XLSSC 102	0.969	1.69	0.574	$3.2^{+0.8}_{-0.5}$	13.31 ± 1.41	16.07 ± 1.70	33.56 ± 3.56
XLSSC 103	0.233	1.12	0.913	$3.5^{+1.2}_{-0.8}$	0.90 ± 0.10	1.30 ± 0.14	3.20 ± 0.35
XLSSC 104	0.294	1.15	1.038	$4.7^{+1.5}_{-1.0}$	0.86 ± 0.10	1.36 ± 0.15	4.36 ± 0.42
XLSSC 105	0.429	1.24	1.024	$5.2^{+1.1}_{-0.8}$	7.91 ± 0.57	12.39 ± 0.89	34.34 ± 2.47
XLSSC 106	0.300	1.16	0.856	$3.3^{+0.4}_{-0.3}$	3.16 ± 0.15	4.44 ± 0.21	10.48 ± 0.49
XLSSC 107	0.436	1.25	0.711	$2.7^{+0.4}_{-0.4}$	3.82 ± 0.32	4.89 ± 0.41	10.33 ± 0.88
XLSSC 108	0.254	1.13	0.705	$2.2^{+0.3}_{-0.2}$	1.49 ± 0.10	1.90 ± 0.13	3.86 ± 0.26
XLSSC 109	0.491	1.29	0.787	$3.4^{+1.3}_{-0.8}$	4.71 ± 0.78	6.30 ± 1.04	14.34 ± 2.37
XLSSC 110	0.445	1.25	0.525	$1.6^{+0.1}_{-0.1}$	1.43 ± 0.22	1.63 ± 0.25	2.82 ± 0.43
XLSSC 111	0.299	1.16	1.017	$4.5^{+0.6}_{-0.5}$	4.27 ± 0.21	6.65 ± 0.32	18.06 ± 0.87
XLSSC 112	0.139	1.07	0.653	$1.8^{+0.2}_{-0.2}$	0.49 ± 0.06	0.61 ± 0.08	1.15 ± 0.15
XLSSC 501	0.333	1.18	0.768	$2.8^{+0.6}_{-0.4}$	1.84 ± 0.22	2.44 ± 0.29	5.34 ± 0.64

Notes. $L_{500,\mathrm{MT}}^{\mathrm{XXL}}$ and $L_{500,\mathrm{MT}}^{\mathrm{bol}}$ are extrapolated out to $r_{500,\mathrm{MT}}$ by integrating under a β-profile (see Sect. 4). [†] Indicates that only a photometric redshift was available for the cluster analysis.

Table 1. continued.

XLSSC Num	z	$E(z)$	$r_{500,MT}$ Mpc	$T_{300\ kpc}$ (keV)	$L^{XXL}_{300\ kpc}$ 10^{43} (erg s^{-1})	$L^{XXL}_{500,MT}$ 10^{43} (erg s^{-1})	$L^{bol}_{500,MT}$ 10^{43} (erg s^{-1})
XLSSC 502	0.141	1.07	0.532	$1.2^{+0.0}_{-0.1}$	0.55 ± 0.04	0.63 ± 0.05	1.00 ± 0.08
XLSSC 503	0.336	1.18	0.642	$2.0^{+0.3}_{-0.2}$	2.01 ± 0.19	2.47 ± 0.24	4.79 ± 0.46
XLSSC 504	0.243	1.12	1.953	$13.8^{+-13.8}_{-5.4}$	0.48 ± 0.17	1.35 ± 0.48	6.87 ± 2.46
XLSSC 505	0.055	1.02	0.661	$1.7^{+0.2}_{-0.1}$	0.38 ± 0.02	0.47 ± 0.03	0.90 ± 0.05
XLSSC 506	0.717	1.49	0.798	$4.5^{+2.1}_{-1.5}$	6.31 ± 1.25	8.53 ± 1.69	20.69 ± 4.08
XLSSC 507	0.566	1.34	0.612	$2.4^{+0.6}_{-0.5}$	3.68 ± 0.63	4.43 ± 0.76	8.77 ± 1.50
XLSSC 508	0.539	1.32	0.742	$3.3^{+0.7}_{-0.5}$	3.48 ± 0.33	4.55 ± 0.43	10.08 ± 0.95
XLSSC 509	0.633	1.39	0.806	$4.2^{+1.1}_{-0.8}$	6.61 ± 0.64	8.99 ± 0.86	21.49 ± 2.07
XLSSC 510	0.394	1.22	0.711	$2.6^{+0.4}_{-0.3}$	2.31 ± 0.16	2.96 ± 0.20	6.22 ± 0.43
XLSSC 511	0.130	1.06	0.545	$1.3^{+0.1}_{-0.1}$	0.25 ± 0.03	0.29 ± 0.04	0.48 ± 0.06
XLSSC 512	0.402	1.22	0.848	$3.6^{+0.6}_{-0.4}$	2.14 ± 0.14	2.99 ± 0.19	7.11 ± 0.46
XLSSC 513	0.378	1.21	0.936	$4.2^{+0.8}_{-0.5}$	4.40 ± 0.30	6.50 ± 0.44	16.63 ± 1.12
XLSSC 514	0.169	1.08	0.582	$1.5^{+0.2}_{-0.1}$	0.40 ± 0.06	0.47 ± 0.07	0.81 ± 0.12
XLSSC 515	0.101	1.05	0.540	$1.2^{+0.1}_{-0.1}$	0.32 ± 0.03	0.37 ± 0.04	0.59 ± 0.06
XLSSC 516	0.866	1.60	0.695	$4.8^{+1.0}_{-0.7}$	18.38 ± 1.97	23.31 ± 2.50	55.21 ± 5.91
XLSSC 517	0.699	1.45	0.698	$3.4^{+1.1}_{-0.6}$	5.77 ± 0.88	7.33 ± 1.12	16.09 ± 2.47
XLSSC 518	0.177	1.09	0.535	$1.3^{+0.0}_{-0.0}$	0.50 ± 0.05	0.58 ± 0.05	0.93 ± 0.09
XLSSC 519	0.270	1.14	0.555	$1.5^{+0.2}_{-0.2}$	0.81 ± 0.15	0.94 ± 0.18	1.59 ± 0.30
XLSSC 520	0.175	1.08	0.805	$2.7^{+0.2}_{-0.1}$	1.72 ± 0.05	2.34 ± 0.07	5.19 ± 0.16
XLSSC 521	0.807	1.54	0.775	$4.7^{+1.3}_{-0.8}$	12.99 ± 1.46	17.32 ± 1.95	42.03 ± 4.72
XLSSC 522	0.395	1.22	0.711	$2.6^{+0.4}_{-0.3}$	2.11 ± 0.15	2.71 ± 0.19	5.69 ± 0.40
XLSSC 523	0.343	1.18	0.779	$2.9^{+0.6}_{-0.4}$	2.17 ± 0.17	2.90 ± 0.23	6.40 ± 0.51
XLSSC 524	0.270	1.14	0.754	$2.6^{+0.5}_{-0.4}$	0.92 ± 0.09	1.21 ± 0.12	2.59 ± 0.25
XLSSC 525	0.379	1.21	0.832	$3.4^{+0.3}_{-0.3}$	4.83 ± 0.24	6.68 ± 0.33	15.54 ± 0.76
XLSSC 526	0.273	1.14	0.794	$2.8^{+0.4}_{-0.2}$	3.91 ± 0.20	5.27 ± 0.27	11.68 ± 0.60
XLSSC 527	0.076	1.03	0.926	$3.1^{+2.8}_{-1.0}$	0.14 ± 0.03	0.20 ± 0.05	0.50 ± 0.12
XLSSC 528	0.302	1.16	0.839	$3.2^{+0.8}_{-0.4}$	1.49 ± 0.11	2.07 ± 0.16	4.82 ± 0.36
XLSSC 529	0.547	1.33	0.769	$3.5^{+0.7}_{-0.4}$	5.20 ± 0.44	6.91 ± 0.58	15.71 ± 1.32
XLSSC 530	0.182	1.09	0.686	$2.0^{+0.2}_{-0.2}$	0.60 ± 0.05	0.75 ± 0.06	1.49 ± 0.13
XLSSC 531	0.391	1.22	0.966	$4.5^{+2.2}_{-1.4}$	1.81 ± 0.25	2.73 ± 0.38	7.18 ± 0.99
XLSSC 532	0.392	1.22	0.772	$3.0^{+0.6}_{-0.5}$	2.58 ± 0.23	3.43 ± 0.31	7.59 ± 0.68
XLSSC 533	0.107	1.05	0.789	$2.4^{+0.1}_{-0.1}$	1.64 ± 0.04	2.21 ± 0.05	4.80 ± 0.12
XLSSC 534	0.853	1.58	0.725	$4.3^{+1.7}_{-1.0}$	12.49 ± 1.87	16.14 ± 2.41	37.74 ± 5.66
XLSSC 535	0.172	1.08	0.756	$2.4^{+0.3}_{-0.2}$	1.83 ± 0.10	2.41 ± 0.13	5.14 ± 0.28
XLSSC 536	0.170	1.08	0.659	$1.8^{+0.3}_{-0.2}$	0.38 ± 0.06	0.47 ± 0.08	0.91 ± 0.14
XLSSC 537	0.515	1.30	0.934	$4.8^{+1.2}_{-0.9}$	5.47 ± 0.45	8.07 ± 0.67	21.11 ± 1.76
XLSSC 538	0.332	1.18	0.804	$3.1^{+0.9}_{-0.6}$	1.35 ± 0.14	1.83 ± 0.19	4.13 ± 0.42
XLSSC 539	0.184	1.09	0.520	$1.2^{+0.1}_{-0.2}$	0.38 ± 0.07	0.44 ± 0.08	0.69 ± 0.12
XLSSC 540	0.414	1.23	0.776	$3.1^{+0.4}_{-0.4}$	4.13 ± 0.25	5.52 ± 0.34	12.31 ± 0.75
XLSSC 541	0.188	1.09	0.805	$2.7^{+0.3}_{-0.3}$	1.05 ± 0.06	1.42 ± 0.09	3.16 ± 0.20
XLSSC 542	0.402	1.22	1.202	$6.8^{+0.5}_{-0.3}$	28.69 ± 0.60	50.37 ± 1.05	157.70 ± 4.59
XLSSC 543	0.381	1.21	0.689	$2.4^{+0.5}_{-0.3}$	1.06 ± 0.14	1.33 ± 0.18	2.73 ± 0.36
XLSSC 544	0.095	1.04	0.788	$2.4^{+0.2}_{-0.2}$	0.57 ± 0.02	0.77 ± 0.03	1.68 ± 0.07
XLSSC 545	0.353	1.19	0.668	$2.2^{+1.6}_{-0.6}$	1.13 ± 0.33	1.41 ± 0.41	2.82 ± 0.81
XLSSC 546	0.792	1.53	0.668	$3.5^{+0.7}_{-0.6}$	10.49 ± 1.09	13.08 ± 1.36	28.47 ± 2.97
XLSSC 547	0.371	1.20	0.920	$4.0^{+1.1}_{-0.8}$	2.80 ± 0.27	4.09 ± 0.40	10.31 ± 1.00
XLSSC 548	0.321	1.18	0.428	$1.0^{+0.1}_{-0.1}$	0.47 ± 0.13	0.51 ± 0.13	0.74 ± 0.19
XLSSC 549	0.808	1.54	0.709	$4.0^{+2.4}_{-0.9}$	8.87 ± 1.50	11.34 ± 1.92	25.92 ± 4.40

3. Analysis

In this section we describe the cluster analysis process used in this work.

The extent of the cluster emission was defined as the radius beyond which no significant cluster emission is detected using a threshold of 0.5σ above the background level. This is intended to provide a conservative estimate of the radius beyond which

there is no significant cluster emission. A one-dimensional (1D) surface brightness profile of each camera was produced. A background annulus was defined with an inner radius of 250″ and modelled by a flat (particle) and vignetted (X-ray) component. The two model components were then fit to the radial profile in the background region using the χ^2 statistic and then summed to produce a total background model. The radial bins were constructed to be 15.4″ in width, chosen to ensure greater than 20 counts per bin and with enough bins to perform the fitting procedure. The radial profile for each camera was then summed to produce an overall profile. An initial source extent was determined based on the 0.5σ radius, and the background fitting repeated using the extent as the inner radius for the background annulus. This process was iterated until the source extent radius changed by less than 1%.

To account for the background in the spectral analysis, local backgrounds were used. However, owing to the survey detection of the clusters, they are detected at a range of off-axis positions on the XMM cameras. Therefore, if possible, an annulus centred on the aimpoint of the observation (BG_{aim}) with a width equal to the diameter of the spectral extraction region was used. This ensures that the local background is taken at the same off-axis position as the cluster, which helps to reduce the systematic uncertainties due to the radial dependencies of the background components. To ensure that no cluster emission was included in the background subtraction, a region centred on the cluster with radius equal to the cluster extent (see above) was excluded. Figure 1 shows an example of this local background for one of our clusters. However, if this method was not possible (owing to close proximity to the aimpoint or a large cluster extent), an annulus centred on the cluster (BG_{clust}) with inner radius equal to the cluster extent and an outer radius of 400″ was used for the local background. The clusters XLSSC 060 and XLSSC 091 had a source extent larger than 400; therefore, an outer radius of 500″ and 800″, respectively, was used for the cluster centred local background.

Cluster spectra were extracted for each of the XMM cameras and fits were performed in the 0.4–7.0 keV band with an absorbed APEC (Smith et al. 2001) model (v2.0.2) with the absorbing column fixed at the Galactic value (Kalberla et al. 2005). The spectra for each camera were fit simultaneously with the temperature of the APEC components tied together. The fits were performed using XSPEC (v12.8.1i) and the abundance table from Anders & Grevesse (1989). Because of the low number of counts for many of the clusters, the spectra were fitted using the cstat statistic. The background spectra were grouped such that they contained at least 5 counts per bin, and this grouping applied to the source spectra. A similar method was employed and justified in Willis et al. (2005) who analysed a sample of 12 galaxy groups and clusters in the XMM-LSS. Throughout the spectral analysis we assumed a fixed metal abundance of $Z = 0.3\,Z_\odot$.

The cluster temperatures are derived within 300 kpc for each cluster, denoted as $T_{300\,kpc}$. This radius represents the largest radius for which a temperature could be derived for the entire cluster sample. The normalisations for each camera were free in the spectral fit, with the pn camera used to calculate the luminosity. We denote the luminosity within 300 kpc as $L_{300\,kpc}^{XXL}$, where the superscript XXL refers to the [0.5–2.0] keV band (cluster rest frame). Luminosities quoted within r_{500} are extrapolated from 300 kpc out to r_{500} by integrating under a β-profile assuming $r_c = 0.15\,r_{500}$ and $\beta = 0.667$. The β-profile parameters were chosen to match those used in Paper II. We note that the uncertainties on the luminosity are scaled by this extrapolation, but do not include any uncertainty on the β-profile parameters. The impact
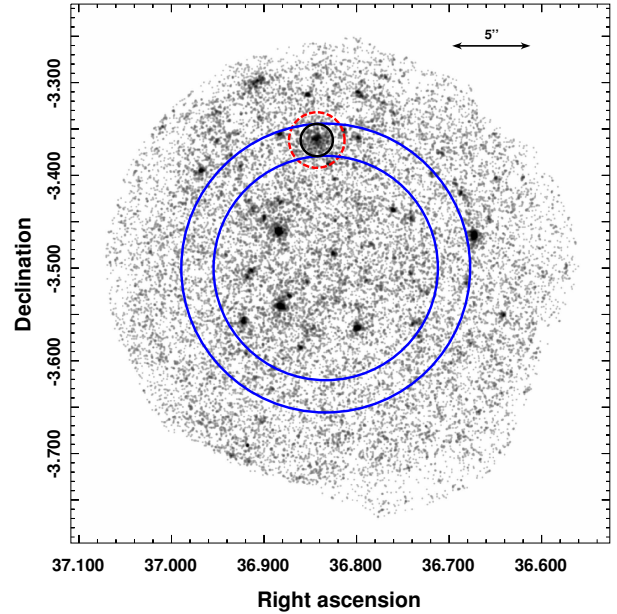
Fig. 1. Example of the background method used in the spectral analysis (see Sect. 3). The image of the cluster XLSSC 010 with the regions showing the spectral extraction region (black circle), cluster detection radius (dashed red circle), and the background annulus centred on the aimpoint of the observation (blue annulus).

of these assumptions is tested in Sect. 5.3.4. Values for cluster r_{500} are calculated using a mass-temperature relation ($r_{500,MT}$, see below). We denote $L_{500,MT}^{XXL}$ as the luminosity in the [0.5–2.0] keV band (cluster rest frame) within $r_{500,MT}$, and $L_{500,MT}^{bol}$ as the bolometric luminosity within $r_{500,MT}$. All the properties quoted include the cluster core because the exclusion of the cluster core is not possible for all 100 clusters. The results of our spectral analysis are given in Table 1. The cluster XLSSC 504 was dropped because of the unconstrained errors reported by XSPEC.

A mass-temperature ($M_{WL} - T$) relation is used in this work for two purposes: (i) to calculate $r_{500,MT}$ for the XXL-100-GC and (ii) to convert the mass function to a temperature function (see Sect. 4.3) for the bias correction. The $M_{WL} - T$ relation is presented in Lieu et al. (2016, hereafter Paper IV), based upon weak lensing cluster masses and the temperatures presented in this work. Briefly, the $M_{WL} - T$ relation was determined using 37 XXL-N clusters that fell within the Canada-France-Hawaii Telescope Lensing Survey (CFHTLenS) footprint, utilising the CFHTLenS shear catalogue (Heymans et al. 2012; Erben et al. 2013) for the mass measurements. In order to increase the statistics and the mass range covered, the XXL-100-GC is combined with 10 groups from the COSMOS survey (Kettula et al. 2013), and 50 massive clusters from the Canadian Cluster Comparison Project (CCCP, Hoekstra et al. 2015).

The combined $M_{WL} - T$ relation is fitted with a power-law of the form (assuming self-similar evolution)

$$\log_{10}(M_{WL} E(z)) = A_{MT} + B_{MT} \log_{10}(T) \qquad (1)$$

using the Bayesian code *linmix_err* (Kelly 2007). In Paper IV we find $A_{MT} = 13.56^{+0.10}_{-0.08}$ and $B_{MT} = 1.69^{+0.12}_{-0.13}$. See Paper IV for further discussions on the results from the $M_{WL} - T$ relation.
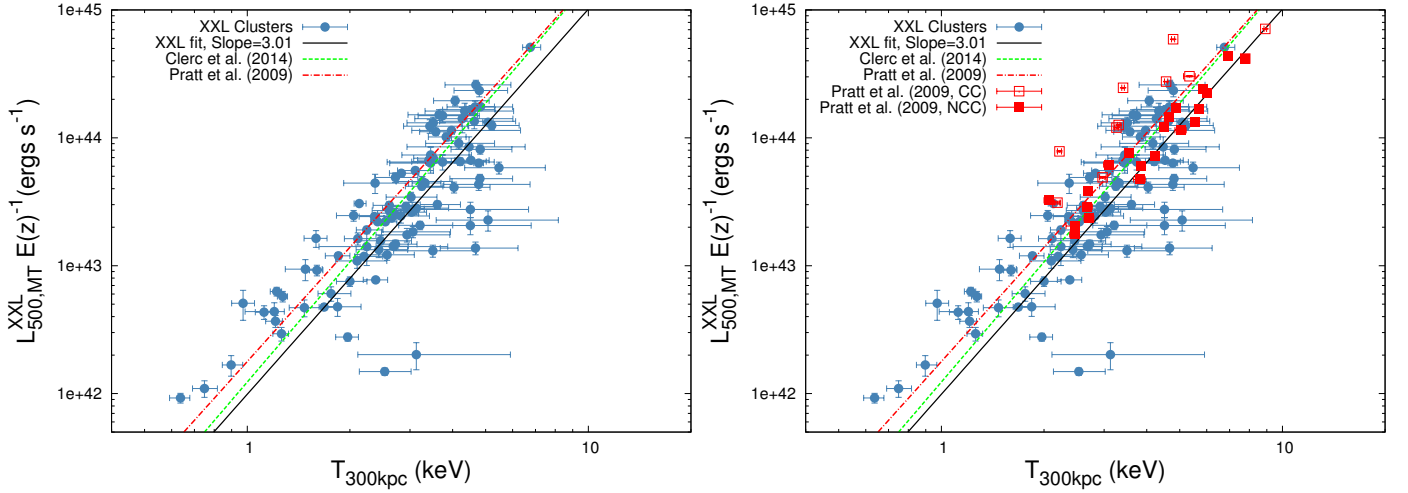
Fig. 2. *Left*: LT relation for the XXL sample. The black line represents an unbiased fit to the data (see Sect. 4.1). The LT relations of Pratt et al. (2009) and Clerc et al. (2014), given by the red dot-dashed line and the green dashed line, respectively, are overplotted; *right*: same as the *left plot*, but with the REXCESS clusters studied in Pratt et al. (2009) overplotted, split between cool-core (open red squares) and non-cool-core (filled red squares) clusters. In both plots, the errors on the temperatures for the XXL clusters have been transformed via the method described in Sect. 4.

4. Results

The results are presented in the form of a study of the LT relation, taking the selection effects fully into account. We present two implementations to account for the selection effects: (i) an updated method of the Pacaud et al. (2007) implementation, defined as the XXL likelihood; and (ii) a method based upon Mantz et al. (2010b), defined as the M10 likelihood. We first present the sample LT relation, not correcting for the selection effects. This allows for comparison of the LT relation when taking into account selection effects, what impact this has on the derived scaling relation, and also for the comparison with previously published relations that do not account for selection effects.

For the analysis of the scaling relations, we account for the fact that the likelihood curve for a measured temperature is approximately Gaussian in log space (consistent with the asymmetric errors usually found in temperature measurements). We use the method of Andreon (2012) to convert the generally asymmetric errors reported by XSPEC into a log-normal likelihood. We note that the errors on the temperature given in Table 1 are those reported by XSPEC.

4.1. Sample LT relation

Figure 2 (left panel) shows the L_{XXL}-T relation for the XXL-100-GC. For simplicity, the L_{XXL}-T notation explicity refers to the $L_{500,MT}^{XXL} - T_{300\,kpc}$ relation. A fit to the data using a power law of the form

$$\left(\frac{L_{XXL}}{L_0}\right) = E(z)^{\gamma_{LT}} A_{LT}\left(\frac{T}{T_0}\right)^{B_{LT}}$$ (2)

was performed, where A_{LT}, B_{LT}, and γ_{LT} represent the normalisation, slope, and power of the evolution correction respectively. We note that the two clusters at low luminosity offset from the L_{XXL}-T are the clusters XLSSC 011 and 527. These clusters are low S/N clusters at low redshift, 0.054 and 0.076, such that the 300 kpc region is large on the detector. The temperature measurement is likely affected by these factors. However, we still include them in the fit to the L_{XXL}-T relation. The power law was fit to the data using the BCES orthogonal regression in base ten log space (Akritas & Bershady 1996) assuming self-similar

evolution. The fit is given by the black solid line in Fig. 2, assuming $L_0 = 3 \times 10^{43}$ erg s^{-1}, $T_0 = 3$ keV, and $\gamma_{LT} = 1$ (self-similar). We find a normalisation of $A_{LT} = 0.90 \pm 0.06$, and slope $B_{LT} = 3.03 \pm 0.27$. For comparison, we fit the LT relation to the 31 REXCESS clusters studied in Pratt et al. (2009, hereafter P09), and 52 clusters selected within the 11 deg^2 XMM-LSS survey (Clerc et al. 2014, hereafter C14). To fit for these LT relations we use the data from Table B1 (Cols. T_1 and $L[0.5-2]_1$) in P09, and the data given in Table 1 (Cols. T_X and $L_{500}^{[0.5-2]}$) in C14. The P09 and C14 relations are hereafter denoted as $L_{P09} - T$ and $L_{C14} - T$, respectively, and the fit parameters are given in Table 2. The fits to the P09 and C14 clusters are given by the red dot-dashed line and green dashed line, respectively, assuming the same L_0, T_0, and γ_{LT} as for the XXL-100-GC fit. We find no significant difference between the XXL-100-GC L_{XXL}-T relation and the $L_{C14} - T$ relation. This is unsurprising as the C14 clusters are selected from the XMM-LSS area, which has many clusters in common with the XXL-100-GC.

We find a 2.8σ difference in the normalisation as compared to the REXCESS clusters, with the XXL normalisation being lower. This is due to the presence of strong cool core clusters in the REXCESS sample. These clusters are apparent as high-luminosity outliers in Fig. 2 (right), which shows the REXCESS clusters plotted on the XXL LT relation. Qualitatively, it is clear that in the absence of these strong cool core clusters, the remaining REXCESS clusters are consistent with the L_{XXL}-T relation. As discussed in Sect. 5.2, the absence of strong cool core clusters from the XXL-100-GC sample is due to a combination of survey geometry and cool core evolution.

4.2. Selection function

Full details of the construction of the selection function are given in Paper II, but the key points are summarised here. The selection function takes into account three aspects of the XXL-100-GC selection, (i) the pipeline detection; (ii) the flux cut of the XXL-100-GC; and (iii) the survey sensitivity. The pipeline detection, i.e. the C1+2 classification in pointing p (denoted $P_{C1+2,p_i}(I|CR_\infty, r_c, RA, Dec)$), was studied in depth in Pacaud et al. (2006) and updated following the methodology of Clerc et al. (2012). We refer the reader to these works for full details.

Table 2. Best-fitting parameters for the LT relations modelled in this work taking the form $L/L_0 = E(z)^{\gamma_{LT}} A_{LT} (T/T_0)^{B_{LT}}$, where $L_0 = 3 \times 10^{43}$ erg s^{-1} and $T_0 = 3$ keV.

Relation (1)	Fit (2)	A_{LT} (3)	B_{LT} (4)	γ_{LT} (5)	σ_{LT} (6)	N_{det} (7)
L_{XXL}-T	BCES	0.90 ± 0.06	3.03 ± 0.28	1.0 (fixed)	0.53 ± 0.07	–
L_{P09}-T	BCES	1.54 ± 0.22	2.97 ± 0.34	1.0 (fixed)	0.62 ± 0.07	–
L_{C14}-T	BCES	1.26 ± 0.25	3.12 ± 0.43	1.0 (fixed)	0.84 ± 0.15	–
L_{XXL}-T	**XXL**	**0.71 ± 0.11**	**2.63 ± 0.15**	**1.64 ± 0.77**	**0.47 ± 0.07**	**117**
L_{bol}-T	XXL	1.21 ± 0.19	3.08 ± 0.15	1.64 ± 0.77	0.47 ± 0.07	–
L_{XXL}-T	M10	0.71 ± 0.10	2.70 ± 0.14	1.27 ± 0.49	0.50 ± 0.06	104

Notes. The fit highlighted in bold represents our main result obtained with the bias correction method described in Sect. 4.3. The bolometric relations are transformed from the soft-band relation via the method described in Sect. 4.7. (1) LT relation; (2) fit method; (3) normalisation; (4) slope; (5) evolution term ($E(z)^{\gamma_{LT}}$); (6) intrinsic scatter; and (7) number of clusters predicted by the model.

The modelling of the flux cut assumes that the errors on the GCA count rate can be modelled as a Gaussian distribution. The probability of a true aperture count rate (CR_{60}) being greater that the count-rate cut (CR_{cut}) for a given pointing (p_i) is

$$P_{P_i}(I|CR_\infty, r_c, RA, Dec) = \frac{P_{C1+2,p_i}(I|CR_\infty, r_c, RA, Dec)}{2}$$

$$\times \left(1 + erf\left[\frac{\epsilon_{60}(r_c)CR_\infty - CR_{cut}}{\sigma_m(\epsilon_{60}(r_c)CR_\infty, RA, Dec)\sqrt{2}}\right]\right), \quad (3)$$

where $\epsilon_{60}(r_c) = \left(1 - \left[1 + (60''/r_c)^2\right]^{1.5-3\beta}\right)$ and CR_∞ is the pipeline count rate extrapolated to infinity. The final ingredient is the modelling of pointing overlaps, where we assume the detection is independent over the different pointings. For a given position, pointings are sorted by increasing off-axis distance, reproducing the overlap cross-matching procedure of the survey. The combined selection function is then given by

$$P(I) = \sum_{i=1}^{N}\left[P_{p_i}(I)\prod_{j<i}\left(1 - P_{C1+2,p_j}(I)\right)\right]. \quad (4)$$

4.3. Likelihood

The observational data used in this study is the distribution of the XXL-100-GC clusters in L, T, and z. Our physical model assumes that the cluster population is described by a power-law correlation between L and T with log-normal scatter in L and evolution in L by $E(z)^{\gamma_{LT}}$. The XXL-100-GC data represent a subset of this population selected according to our selection function and with noisy measurements of L and T, denoted $\hat{L}$ and $\hat{T}$. We neglect any measurement errors on z.

The number density of clusters in the survey volume is taken into account by using a mass function, assumed to be described by a Tinker mass function (Tinker et al. 2008). We then transform this to a temperature function, dn/dT, using the $M_{WL}-T$ relation given in Sect. 3. In the present analysis we neglect the intrinsic scatter in the $M_{WL}-T$ relation, and the measurement errors on the parameters of the scaling relation, and assume that its evolution is self-similar (i.e. $M \propto E(z)T^{B_{MT}}$).

The total number of clusters N in the volume is then the integral over the temperature and redshift range considered, multiplied by the solid angle of the survey Ω:

$$\langle N \rangle = \Omega \int dT \int dz \frac{dn}{dT}\frac{dVd\Omega}{dz}. \quad (5)$$

The number of clusters predicted by our model to be *observed* in the subsample defined by our selection function is the integral of the mass function over the volume of the survey, weighted by the probability that a cluster of a given mass would be included in the subsample given the LT relation and the intrinsic and statistical scatter on the luminosity,

$$\langle N_{det} \rangle = \int dT \int dz \frac{dn}{dT}\frac{dVd\Omega}{dz}\Omega$$

$$\times \int dL\, P(L|T,z,\theta) \times P(I|L,T,z), \quad (6)$$

where θ stands for our full set of model parameters ($A_{LT}, B_{LT}, \gamma_{LT}, \sigma_{LT}$) describing the LT relation. In this expression, the first probability, $P(L|T,z,\theta)$, is the probability that cluster of temperature T has some intrinsically scattered luminosity. The second probability, $P(I|L,T,z)$, is the selection function, i.e. the probability that a cluster with a luminosity L and temperature T at a redshift z would be included in the subsample. This is summarised in Sect. 4.2. We note the change in notation as we are writing the likelihood in terms of the cluster properties L and T.

The (un-normalised) likelihood of a cluster i in our sample having the observed properties ($\hat{L}_i, \hat{T}_i$) is given by

$$P_i(\hat{L}_i, \hat{T}_i, I|z_i, \theta) = \int dT \int dL \frac{\frac{dn}{dT}\frac{dVd\Omega}{dz}\Omega}{\langle N \rangle}$$

$$\times P(L|T,z,\theta)P(\hat{L}|L)P(\hat{T}|T)P(I|L,T,z). \quad (7)$$

The inclusion of $\langle N \rangle$ normalises the temperature function to a probability distribution for an arbitrary cluster to have a temperature T at redshift z. The probability of $P(L|T,z)$ is as defined above, and the remaining terms are the probability of each of the observables using the measured uncertainty for that observable. The joint probability of the full set of observed cluster properties is the product of $P_i(\hat{L}, \hat{T})$ over all N_{det} observed clusters in the sample.

Equation (7) is an improper probability because $P(I|L,T,z)$ does not integrate to unity, and it does not penalise the model for predicting the existence of clusters in parts of the L, T, z space where they are within the selection function but are not observed. In other words, the model is not penalised for excess probability density in regions of the space where the lack of detections disfavours the existence of clusters. This is resolved by normalising Eq. (7) by the integral over the observed $\hat{L}, \hat{T}$ space to give the final likelihood

$$\mathcal{L}(\hat{L}, \hat{T}, I|z, \theta) = \prod_{i}^{N_{det}} \frac{P_i(\hat{L}, \hat{T}, I|z_i, \theta)}{\int d\hat{T} \int d\hat{L}\, P_i(\hat{L}, \hat{T}, I|z_i, \theta)}. \quad (8)$$

This normalisation penalises the model for excess probability density in regions of the parameter space where the data disfavour the existence of clusters. For example, we consider a set of model parameters that give a good fit to the properties of the observed clusters, but also give a high probability of cool, highly luminous clusters, when none are observed. This would lead to a larger denominator in Eq. (7), and hence a lower overall likelihood compared with an alternate set of parameters that describes the properties of the observed clusters equally well, but does not predict the unobserved clusters. This likelihood is referred to as the XXL likelihood.

We also consider an alternative construction of the likelihood set out by M10. In this approach, the final likelihood for the sample of clusters and their observed properties is the product of a Poisson likelihood of N total clusters (detected plus undetected) given the model prediction $\langle N \rangle$, a binomial coefficient accounting for the number of ways of drawing N_{det} detected clusters from the total N, the joint probability of the set of observed cluster properties (the product of Eq. (7) over the N_{det} clusters), and the probability of not detecting the remaining $N - N_{det}$ clusters. Neglecting terms not dependent on the model parameters, the likelihood simplifies to

$$\mathcal{L}(\hat{L}, \hat{T}, I | z, \theta) \propto e^{-\langle N_{det} \rangle} \prod_{i=1}^{N_{det}} \langle \tilde{n}_{det,i} \rangle, \qquad (9)$$

where $\langle \tilde{n}_{det,i} \rangle = P(\hat{L}, \hat{T}) \langle N \rangle$ for the ith cluster.

The principal difference between Eqs. (8) and (9) is that the latter has a stronger requirement that the model must accurately predict the number of observed clusters in addition to their distribution in (L, T, z). This has the advantage that it uses additional information to constrain the model, and is a requirement when the analysis is being used to constrain cosmology in addition to the form of the scaling relations, as in M10.

However, when the aim of the analysis is to infer the form of the scaling relations under an assumed cosmology, Eq. (8) has certain advantages. This implementation is insensitive to systematics affecting the numbers of clusters (such as the normalisation of the mass function and hence σ_8) or the normalisation of the MT relation, and so gives more robust measurements of the scaling relation parameters. Furthermore, since the number of observed clusters is not used to constrain the model parameters in this approach, the number of detected clusters can be used as a posterior predictive check.

4.4. Inference of model parameters

The likelihood of Eq. (7) was combined with priors on each of the model parameters to compute the posterior probability. The priors used were uniform in the range $(-\infty, \infty)$ for A_{LT}, B_{LT}, and γ_{LT} and uniform in the range $(0.01, 2.0)$ for σ_{LT} (expressed in natural log, so representing fractional scatter).

The posterior distribution was analysed using the Bayesian inference package *Laplace's Demon*[2] within the *R* statistical computing environment (R Core Team 2014). The posterior distribution was first explored using a Laplace approximation for computational efficiency before refining the fit using an MCMC algorithm. We used the Adaptive Metropolis-within-Gibbs algorithm in *Laplace's Demon* for this purpose, and used four parallel chains of 50 000 iterations each, initialised to randomised starting values (near the mode of the posterior identified by the Laplace approximation). The stationary parts of the chains

---

[2] http://www.bayesian-inference.com/software
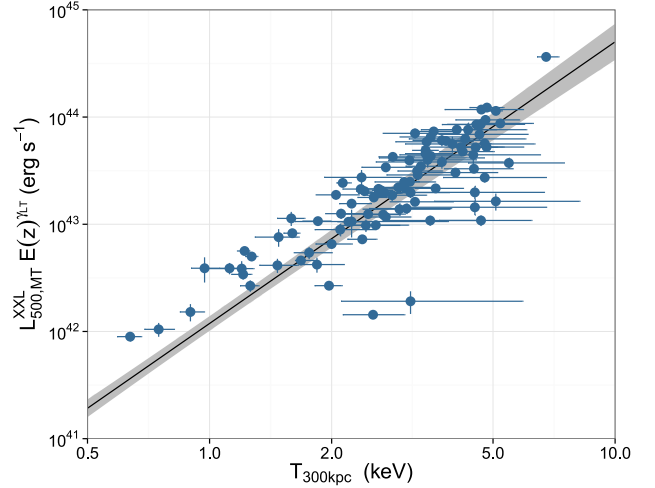
Fig. 3. L_{XXL}-T relation with the best-fitting model. The light blue circles show the XXL-100-GC clusters; the best-fitting model is shown as the solid black line the 1σ uncertainty represented by the grey shaded region.

were compared using the Gelman and Rubin (1992) convergence diagnostic, and the largest value of the 95% upper bound on the potential scale reduction factor was 1.01, giving a strong indication that the chains had converged. The stationary parts of the chains were then concatenated giving an effective sample size of at least 500 for each parameter.

4.5. The L_{XXL}-T relation

The L_{XXL}-T relation is plotted in Fig. 3 along with the best-fitting model (black line). The best-fitting parameter values and their uncertainties are then summarised by the mean and standard deviation of the posterior chains for each parameter. The values are given in Table 2, and illustrated with the scatterplot matrix in Fig. 5. We focus our attention on the XXL likelihood method, noting that the results do not change significantly between the XXL and M10 methods. Using the XXL likelihood method, we find a normalisation and slope of $A_{LT} = 0.71 \pm 0.11$ and $B_{LT} = 2.63 \pm 0.15$, respectively. We find a shallower slope than that found when using the BCES regression fit (which did not account for biases, see Sect. 4.1), although the difference in slope is only significant at the 1σ level. The L_{XXL}-T relation is consistent with recent results which also accounts for selection biases. Bharadwaj et al. (2015) studied the LT relation of 26 groups (spanning the $0.6 < T < 3.6$ keV range) and found a slope of $B_{LT,B14} \approx 2.7$, converting their LT relation from bolometric to the soft band (see Sect. 4.7). The comparison is complicated, however, owing to the differing implementations of the bias-correction and fitting methods used in Bharadwaj et al. (2015) and in our work. Interestingly, they find that the slope of the sample LT relation is shallower than the bias-corrected fit, opposite to what we find in this work. However, this could be driven by the large number of strong cool core (SCC) systems in their sample ($\approx 50\%$); the SCC LT relation shows a change in slope from 2.56 ± 0.22 to 3.60 ± 0.22 when correcting for biases.

Next we focus on the evolution of the L_{XXL}-T relation, γ_{LT}, where the evolution is expressed as $E(z)^{\gamma_{LT}}$. For the first time we are able to measure the evolution of the LT relation using clusters drawn from a single homogeneous survey, fully accounting for selection biases. As introduced previously, we expect $\gamma_{LT} = 1$ for strong self-similar evolution, and $\gamma_{LT} = 0.42$ for weak
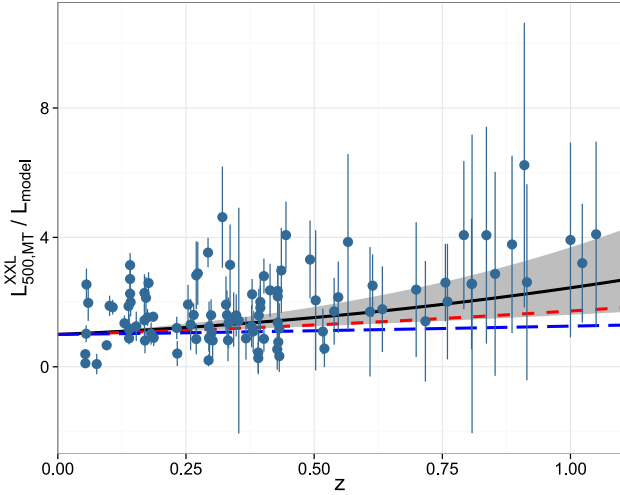
Fig. 4. Evolution of the L_{XXL}-T relation for the XXL-100-GC. The XXL-100-GC are represented by the light blue circles and the best-fitting model is given by the black solid line; the grey shaded region highlights the 1σ uncertainty. The "strong" and "weak" self-similar expectations are given by the red dashed and blue dashed lines, respectively.

self-similar evolution. We find $\gamma_{LT} = 1.64 \pm 0.77$, fully consistent with both the the strong and weak self-similar evolution models. Figure 4 plots the evolution of the LT relation as inferred from our best-fitting model. The best-fit evolution is given by the black solid line along with the 1σ uncertainty, the strong and weak self-similar expectations are given by the red and blue dashed lines, respectively. Our best-fit model appears to lie below all the high-redshift clusters, due to the fit being driven by the larger number of lower redshift clusters. However, the evolution favoured by our best-fit model is in tension with other recent results, and is discussed further in Sect. 5.1.

4.6. Posterior predictive checks

While the modelling process described above determines the best-fitting values of the model parameters for the chosen model, it does not guarantee that the model is a good description of the data. For this we use three types of posterior predictive check to assess how well the final model describes the data.

First, we make visual comparisons of the population of clusters predicted by the best-fitting model and those observed. To do this, a large number of model clusters were generated using the best-fitting model parameters, and including the selection function. Figure 6 shows contours of the simulated population along with the observed clusters in different projections of the observed properties. Figure 7, instead, shows histograms of the simulated and observed properties. In all cases the visual agreement is good.

The second test was to compare the number of clusters predicted to be observed by the best-fitting model with the number observed. The model predicted 116.7 clusters, so the probability of observing a sample as discrepant as or more discrepant than the 99 clusters observed is the sum of the Poisson probabilities $P(N < 99|116.7) + P(N > 134|116.7) = 0.11$. The number of observed clusters is thus reasonably consistent with the number predicted. We emphasise that this is not trivial, as the model is not required to reproduce the number of observed clusters in our likelihood.

The final test we make is to measure the posterior predictive p-value (Meng 1994). This is done by measuring the discrepancy of the data with the model for a set of the model parameters taken from the posterior distribution, and doing the same for a simulated data set generated from the same model parameters. This is repeated for a large number of sets of parameters sampled from the posterior, and the fraction of instances in which the simulated points are more discrepant than the observed data is the posterior predictive p-value. A small fraction indicates that the model is a poor description of the data.

To implement this, we used the χ^2 statistic to measure the discrepancy between the observed or simulated data and the model (as in e.g. Andreon 2012). We scale the luminosity of each point by $E(z)^{\gamma_{LT}}$ for the value of γ_{LT} currently considered and use the modified χ^2 described in Press et al. (1986), which includes the uncertainties in both L and T. For each sample of parameter values, a simulated population of 99 clusters was generated and measurement errors were assigned by taking the log-space errors from a cluster randomly selected from the observed data; the corresponding statistical scatter was then added. This sampling of errors is justified, since we find no dependency of the size of the errors on the measured parameters.

This procedure was repeated for 1000 samples from the posterior; in 19% of those iterations the simulated data were more discrepant than the observed data. We thus conclude that there is no strong evidence for the data to reject our model.

4.7. The L_{bol}-T relation

So far we have been considering the scaling of soft-band luminosity with temperature, but it is often useful to refer to the bolometric luminosity, L_{bol}. We can convert the L_{XXL}-T relation to an $L_{bol} - T$ relation by using a k-correction.

Using XSPEC simulations, we find this k-correction can be approximated by

$$\frac{L_{XXL}}{L_{bol}} = A_k T^{B_k} \tag{10}$$

with $A_k = 0.587$ and $B_k = -0.450$. This power law approximates the k-correction to within $\lesssim 3\%$ over the temperature range of our sample. Substituting into the LT relation we get the bolometric relation:

$$\frac{L_{bol}}{L_0} = E(z)^{\gamma_{LT}} A_{LT} A_k^{-1} \left(\frac{T}{T_0}\right)^{B_{LT}} T^{-B_k} \tag{11}$$

$$= E(z)^{\gamma_{LT}} A_{LT,bol} T_0^{B_k} \left(\frac{T}{T_0}\right)^{B_{LT,bol}} . \tag{12}$$

The L_{bol}-T relation is shown in Fig. 8; the best-fitting model coefficients are given in Table 2.

5. Discussion

In this work we have shown that the evolution of the LT relation is consistent with the strong and weak self-similar expectation (see Sect. 4.5). However, our best-fit evolution is not in agreement with previous studies, and therefore warrants further discussion. We will compare our results with other observational and theoretical work and examine systematics in our analysis that could influence the measured evolution.
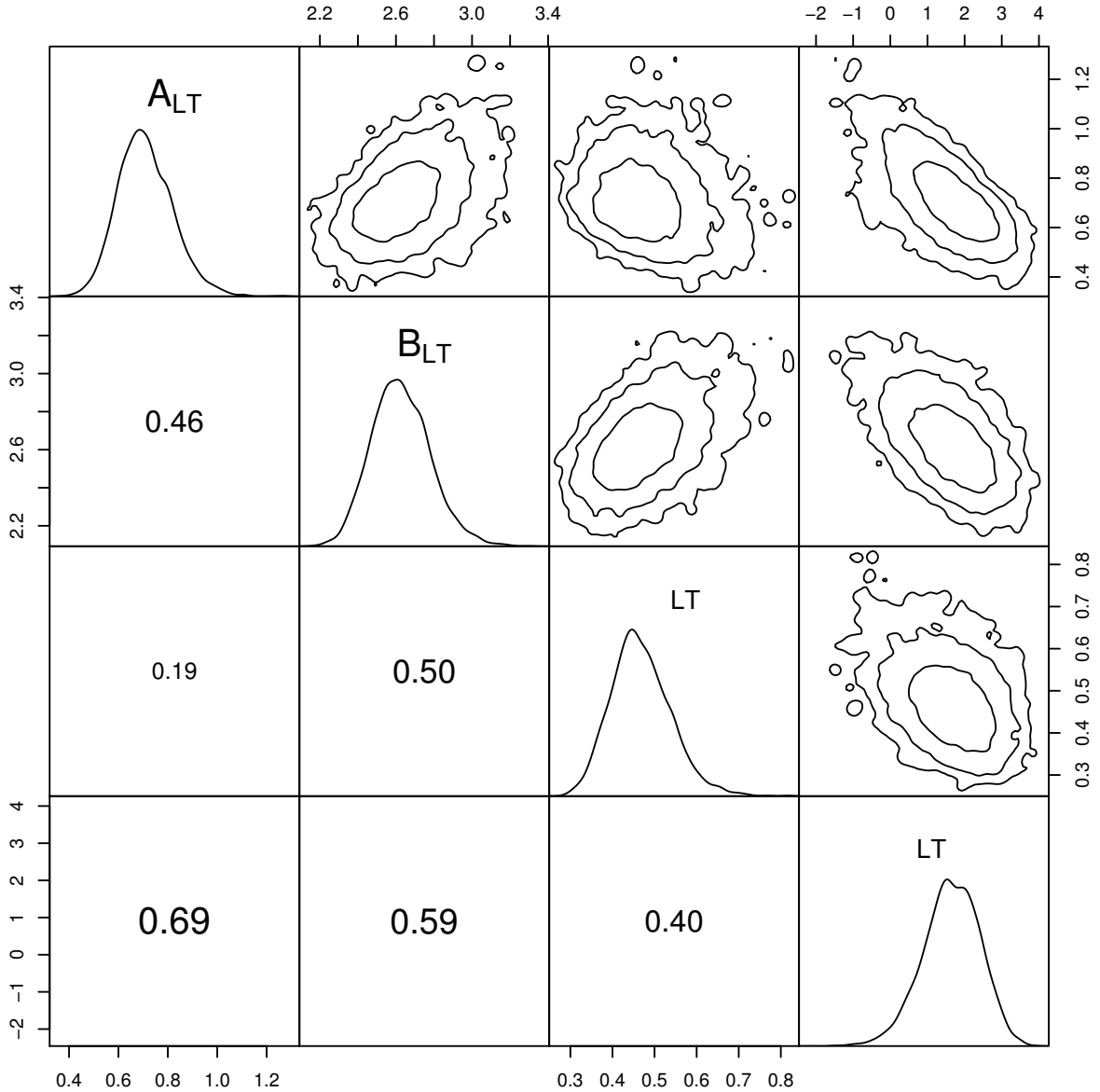
Fig. 5. Scatterplot matrix for the fit of the L_{XXL}-T relation of the XXL-100-GC sample. The posterior densities are shown along the diagonal; the 1σ, 2σ, and 3σ confidence contours for the pairs of parameters are shown in the *upper right panels*. The *lower left panels* show the Pearson's correlation coefficient for the corresponding pair of parameters (text size is proportional to the correlation strength).

5.1. Comparison with other observational studies

We found that the normalisation of the L_{XXL}-T relation evolves as $E(z)^{1.27\pm0.82}$ (Sect. 4.5). This would indicate that clusters are more luminous as a function of increasing redshift for a given temperature. Our result, however, does not agree with recent studies that find a negative evolution (Reichert et al. 2011; Hilton et al. 2012; C14).

The discrepancy with C14 is surprising, given the overlap in the clusters used from the XMM-LSS and that they account for selection effects. Clerc et al. (2014) find a negative evolution when using various local baseline LT relations. Assuming the normalisation of the LT relation evolves as $E(z)(1+z)^{\alpha_{LT}}$, they find $\alpha_{LT} = -2.5 \pm 0.4$ and $\alpha_{LT} = -1.6 \pm 0.4$ when using the P09 and Maughan et al. (2012) LT relations as local baselines. The differences in the assumptions made in C14 and this work are the likely cause of the discrepancy. These assumptions are (i) the local relation used as a reference for comparison to

the high-redshift clusters; (ii) the choice of MT relation to determine r_{500} and hence L_{500}; C14 use the MT relation of Sun et al. (2009), whereas we use the internally calibrated relation in Sect. 3; (iii) the value of r_c, where Clerc et al. (2014) use $r_c = 180$ kpc and we use $r_c = 0.15r_{500}$; and (iv) C14 use the likelihood from Pacaud et al. (2007) for their bias correction, which does not account for the mass function.

To test the dependence of the fit to these assumptions, we repeated the fit using assumptions close to those in (i)–(iii). For this comparison we use the LT relation of P09 for a local baseline, which gave the strongest change in evolution found in C14. We found that we recover a consistent, strong negative evolution on LT as found in C14 when using the same assumptions on the local LT relation, r_c, and MT relation. However, given the small dependence of the results on the assumed x_{500} (defined as the ratio of r_c and r_{500}) and MT relation (see Sect. 5.3 below), the difference in evolution is likely driven by the assumed local LT relation. This shows that differences in the local
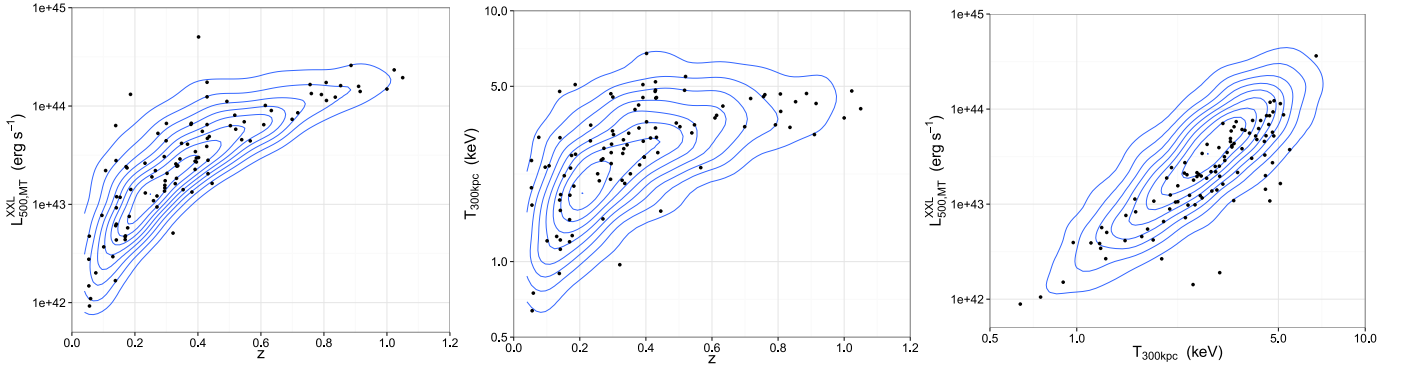
Fig. 6. Contours of the simulated clusters generated from the best-fitting model are plotted in the L, z (*left panel*); T, z (*middle panel*); and L, T (*right panel*) planes, along with points indicating the observed clusters.
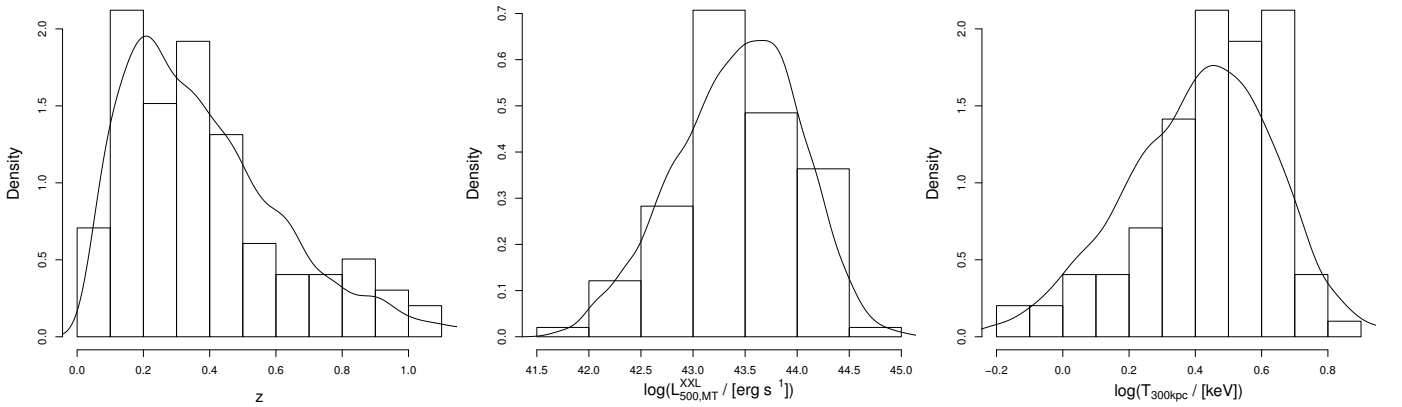
Fig. 7. Histograms of the redshift (*left panel*), luminosity (*middle panel*), and temperature (*right panel*) of the observed clusters are plotted along with the density distribution of the same properties from the simulated clusters generated from the best-fitting model. The histograms and curves are normalised to a total area of 1.
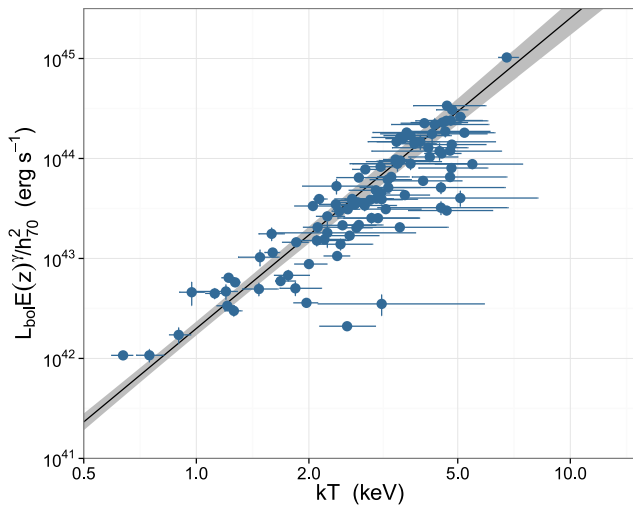
Fig. 8. L_{bol}-T relation with best-fitting model. Our best-fitting model is shown as the solid black line with the grey shading indicating the 1σ uncertainty. The best-fitting model is transformed from the soft band to bolometric via the steps described in Sect. 4.7.

LT relation, of less than 3σ (see Sect. 4.1), can change the form of the LT relation evolution from positive to negative. As we discuss in Sect. 5.2, this effect appears to be driven by the differing cool core populations in the samples used for the local LT relation.

Many studies investigating the evolution of the LT relation, use an external local baseline with which to compare the normalisation of the LT relation. This complicates the interpretation of departures from self-similar evolution, and can change the form of the evolution (see above). Hilton et al. (2012) investigated the evolution of the LT relation using a complete sample of 211 clusters drawn from the XMM Cluster Survey (XCS Romer et al. 2001). Using an internally calibrated LT relation, they find a negatively evolving LT relation of the form $(1 + z)^{-1.5\pm0.5}$. This is again in disagreement with the positive evolution found in this work; however, we note that the Hilton et al. (2012) results do not account for selection biases as we have done here.

5.2. Impact of cool cores

The evolving cool core population in clusters complicates the interpretation of the evolution in the LT relation. Cooling is not present in the self-similar model, and so a reduction in the number or strength of cool cores at high redshift (McDonald et al. 2014) would manifest as weaker than self-similar evolution. As we saw in Sect. 5.1, using an external sample which contains a larger number of strong cool core clusters (such as P09; see our Fig. 2, right plot) strongly affects the magnitude and sign of the measured evolution. It is thus possible that previous measurements of negative evolution in the core-included LT relation mainly reflect the decreasing contribution of cool cores to cluster luminosities at high redshift. An evolving mass-dependence of the prevalence and strength of cool cores would further complicate the interpretation.

Table 3. Best-fitting parameters for the LT relation while varying some assumptions in the model.

Relation	Fit	Assumption	A_{LT}	B_{LT}	γ_{LT}	σ_{LT}	N_{det}
(1)	(2)	(3)	(4)	(5)	(6)	(7)	(8)
L_{XXL}-T	XXL	$x_{500} = 0.1$	0.63 ± 0.10	2.58 ± 0.17	1.58 ± 0.85	0.48 ± 0.08	117
L_{XXL}-T	XXL	$x_{500} = 0.2$	0.81 ± 0.13	2.66 ± 0.15	1.63 ± 0.75	0.45 ± 0.07	115
L_{XXL}-T	XXL	MT†	0.66 ± 0.09	2.47 ± 0.14	2.09 ± 0.65	0.44 ± 0.06	178
L_{XXL}-T	M10	MT†	0.64 ± 0.10	2.65 ± 0.15	0.59 ± 0.54	0.59 ± 0.07	114

Notes. (1) LT relation; (2) fit method; (3) assumption changed; (4) normalisation; (5) slope; (6) evolution term ($E(z)^{\gamma_{LT}}$); (7) scatter; and (8) number of clusters predicted by the model. $^{(\dagger)}$ Denotes the use of the Arnaud et al. (2005) MT relation.

The P09 sample appears to contain a population of strong cool-core clusters, which could drive the regression fit to a higher normalisation not seen in the XXL-100-GC sample. This is likely due to a combination of the evolving cool core population and the geometries of the two surveys. The REXCESS clusters were selected from REFLEX (Böhringer et al. 2001), a flux-limited ($F \times [0.1-2.4 \text{ keV}] \geq 3 \times 10^{-12} \text{ ergs s}^{-1} \text{ cm}^{-12}$) wide area ($\approx 14\,000 \text{ deg}^2$) cluster survey sensitive primarily to high-luminosity clusters at redshifts $z \lesssim 0.25$, while XXL has a much smaller local volume sensitive to lower luminosity clusters than REFLEX. This result was found in Paper II (see Fig. 16), where our data was compared to REFLEX-II (Böhringer et al. 2013).

To explain the apparent lack of strong cool core clusters in the XXL-100-GC sample, we make the simplifying assumptions that the cool core clusters in the P09 sample are uniformly distributed in volume out to $z = 0.2$ (the limit of the REXCESS sample). The total volume of the REXCESS sample selection was calculated from the conditions given in Table 1 of Böhringer et al. (2007). From the ten cool core clusters classified in P09, we would expect an average of one cool core cluster per $1.1 \times 10^8 \text{ Mpc}^3$. When applying this to the 50 deg^2 area of XXL out to $z = 0.2$, we would expect ≈ 0.03 strong cool core clusters.

Thus, the evolution measured in the L_{XXL}-T relation is not confounded by the changing cool core population, and arguably probes the evolution of the baryon content of the clusters more cleanly than studies which compare high-z clusters from small area surveys with low-redshift samples from wide area surveys.

5.3. Systematic effects

Here we investigate the dependence on the model fit to assumptions made in this work.

5.3.1. The choice of x_{500}

One assumption that could have an effect on the L_{XXL}-T relation and its evolution is the relation between r_c and $r_{500,MT}$ (where we adopt $x_{500} = 0.15$). To test the dependence of the fit on the assumed x_{500}, we repeated the fit for $x_{500} = 0.1$ and $x_{500} = 0.2$. The results are given in Table 3 and show no significant difference in the fit parameters when x_{500} is varied in this range. However, x_{500} is assumed to be independent of mass and redshift, but this definition introduces a dependence of the physical size of r_c on mass and redshift, in line with self-similar expectations. Given the decreasing fraction of sharply peaked cool-cores with increasing redshift (Vikhlinin et al. 2007; Santos et al. 2011; Mann & Ebeling 2012; McDonald et al. 2014), one could expect that the average r_c value would increase with redshift. Hudson et al. (2010) found that there was a trend, albeit with

large scatter, between r_c and the central cooling time (CCT) for their sample of 64 HIFLUGS clusters. The CCT is a robust proxy for the presence of a cool-core, and therefore this trend indicates that r_c increases from CC to NCC clusters (see Fig. 6b in Hudson et al. 2010). Furthermore, Hudson et al. (2010) note a temperature dependence on r_c such that cooler clusters appear to have smaller values of x_{500} compared to hotter clusters. Figure 6 shows the temperature-z distribution of our clusters, highlighting how the median cluster temperature in the sample increases with redshift. Depending on the strength of the x_{500}-temperature relation, we could be artificially introducing an evolution on x_{500}. Coupled with the r_c-CC/NCC dependance, we are most likely underestimating the value of x_{500} for the high-redshift clusters. This would lead us to underestimate the luminosities of the high-redshift clusters, steepening the slope of the LT relation. This would lead to the evolution of the LT relation being underestimated.

5.3.2. The choice of MT relation

The choice of MT relation will also have an impact on our results. The MT relation is used (i) to calculate $r_{500,MT}$ for the cluster sample and (ii) to convert the mass function to a temperature function (using the $M_{WL}-T$ relation, see Sect. 4.3). Throughout, we have used the $M_{WL}-T$ relation presented in Paper IV based on XXL+COSMOS+CCCP clusters. To test the dependence of the fitted LT relation to the choice of MT relation, we repeat the fit using the MT relation of Arnaud et al. (2005), which has a similar slope to our $M_{WL}-T$ relation but is $\approx 20\%$ lower in normalisation at 3 keV. The results are given in Table 3. We find that the fit using the XXL likelihood does not change significantly when using the Arnaud et al. (2005) MT relation. However, the fit performed using the M10 likelihood with the Arnaud et al. (2005) MT relation, would imply weaker than self-similar evolution of the LT relation. Because of the large errors on γ_{LT}, the difference is only significant at the $\sim 1\sigma$ level. Furthermore, as a result of the overprediction of the number of clusters in the M10 fit (a requirement of the M10 likelihood), this fit is not an accurate description of the data. The predicted number of clusters from the M10 fit using the Arnaud et al. (2005) MT relation, 114 clusters, does not agree with the observed number of 99 found using the Poisson calculation as above (see Sect. 4.6). We note that the XXL likelihood strongly disfavours the use of the Arnaud et al. (2005) MT relation in the context of the overall model because of the 178 predicted clusters. This shows that the XXL method is less sensitive to changes in the MT relation than the M10 fitting method. However, because of the large errors, drawing conclusions on the effects of the choice of MT relation and likelihood model on γ_{LT} will require many more clusters than contained in the XXL-100-GC sample.
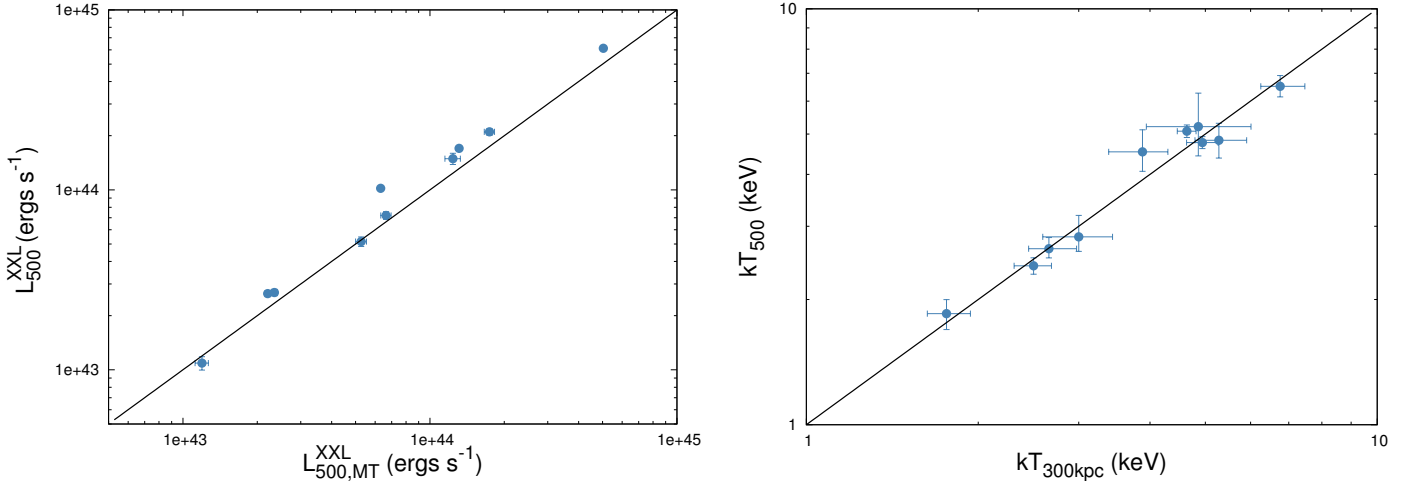
Fig. 9. *Left*: comparison of the luminosity extrapolated out to r_{500} ($L_{500,\mathrm{MT}}^{\mathrm{XXL}}$) to that determined from a spectral analysis within r_{500} (L_{500}^{XXL}). *Right*: comparison of the temperature derived within 300 kpc ($T_{300\,\mathrm{kpc}}$) to the temperature derived within r_{500} (T_{500}). The black line represents a 1:1 relation.

5.3.3. The role of scatter

Even with our efforts to model the impact of selection bias on the LT relation and its evolution, we have made the simplifying assumption that the scatter in the LT relation is independent of both mass and redshift. There is evidence to suggest that the scatter in luminosity for a given temperature or mass decreases for higher redshift systems (Maughan 2007, although this analysis did not account for selection effects). This can be understood from the decline of strong cool core systems towards higher redshift (e.g. McDonald et al. 2014).

Because the higher redshift clusters in our sample have higher temperatures on average, the decreasing cool core fraction leads to a decreasing scatter in L at a given T for the higher redshift part of our sample. Therefore, our model, which assumes a constant scatter, may overestimate the scatter in the high-z population. This would lead to the evolution of the L_{XXL}-T relation being underestimated since a lower scatter would require stronger positive evolution to reproduce the observed luminous high-redshift clusters.

5.3.4. The extrapolation out to r_{500}

Throughout this work we have used a spectral extraction region of 300 kpc for the cluster analysis. This was chosen because a spectral analysis within r_{500} could not be achieved for the majority of the cluster sample. The luminosities are determined within 300 kpc, and extrapolated out to an estimate of r_{500} by integrating under a β-profile (see Sect. 3). We investigate here what systematic effect this could have on the derived luminosities by comparing the extrapolated luminosities ($L_{500,\mathrm{MT}}^{\mathrm{XXL}}$) with those determined via a spectral analysis within r_{500} (L_{500}^{XXL}) for the brightest clusters in the sample. We also compare the temperature derived within 300 kpc ($T_{300\,kpc}$) with that derived within r_{500} (T_{500}) to check for any systematic effects.

We estimate r_{500} via an iterative process based on the MT relation in Paper IV. An initial temperature of 2 keV is used to calculate an initial r_{500}, a spectrum is extracted, and a temperature determined. A new r_{500} is calculated from this temperature, and the process is iterated until r_{500} changes by less than 1%. The left plot in Fig. 9 compares $L_{500,\mathrm{MT}}^{\mathrm{XXL}}$ to L_{500}^{XXL} for the ten highest flux clusters in the XXL-100-GC for which the iteration

process could be performed. We find good agreement between the luminosities for low-luminosity clusters ($\lesssim 7 \times 10^{43}$ erg s^{-1}). However, for higher luminosity clusters ($\gtrsim 7 \times 10^{43}$ erg s^{-1}) we find evidence that $L_{500,\mathrm{MT}}^{\mathrm{XXL}}$ could be underestimated.

Because of the extrapolation out to r_{500}, the values of $L_{500,\mathrm{MT}}^{\mathrm{XXL}}$ would be underestimated by either i) underestimating the value of x_{500} and hence r_c or ii) overestimating the value of β. Section 5.3.1 explored recent evidence for a trend of r_c with increasing temperature, hence increasing luminosity. The increase in r_c with increasing luminosity would explain the underestimate of $L_{500,\mathrm{MT}}^{\mathrm{XXL}}$ compared to L_{500}^{XXL}, hence leading to an underestimate of the evolution of the LT relation (as stated in Sect. 5.3.1).

The right plot in Fig. 9 compares $T_{300\,\mathrm{kpc}}$ to T_{500}. We find no systematic differences between the two temperatures; therefore, we can assume that $T_{300\,\mathrm{kpc}}$ represents the global temperature.

### 5.4. Do the data require γ_{LT} as a free parameter?

Our best-fitting evolution is consistent with strong self-similar evolution, but only stronger than the weak self similar prediction at the $\sim 1\sigma$ level. One may question whether we are justified in fitting for the evolution at all. In other words, compared with a model with fixed self-similar evolution, is the improvement in the fit when we add the additional flexibility to the model to fit the evolution sufficiently large to justify the extra complexity in the model?

There are several ways to address this in a Bayesian framework, and we adopted the deviance information criteria (DIC Spiegelhalter et al. 2002; Liddle 2007). The DIC can be computed for different models and the model with the lowest DIC is preferred by the data with a degree of support determined by the difference in DIC between competing models. The deviance is defined as $D = -2 \ln \mathcal{L}$ and the DIC is then given by

$$\mathrm{DIC} = \bar{D} + p_D, \qquad (13)$$

where $\bar{D}$ is the mean of the deviance computed over the MCMC chain, and p_D is a measure of the effective number of parameters of the model. The latter term penalises more complex models, and is given by

$$p_D = \bar{D} - D(\bar{\theta}). \qquad (14)$$
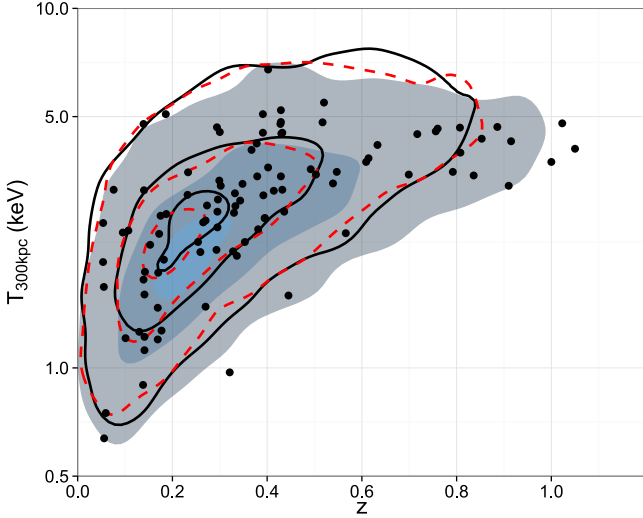
Fig. 10. Contours of the simulated clusters generated from our free-evolution (shaded contours), strong self-similar (black solid contours), and weak self-similar (red dashed contours) evolution models (see Sect. 5.4). Solid black points indicate the observed clusters in our sample.

The term $D(\bar{\theta})$ is the deviance computed at the mean parameter values from the MCMC chain.

The DIC was computed for models with γ_{LT} as a free parameter fixed at the strong and weak self-similar values of 1 and 0.42, respectively. In both cases, the difference between the free-evolution model and the fixed evolution models was greater than -1. Conventionally, differences in DIC more negative than -5 are taken as strong evidence of the more complex model. Our analysis suggests therefore that while the data are better described by the free-evolution model (i.e. $\bar{D}$ is lower), the improvement is not sufficient to give strong support for including evolution as a free parameter.

While the data as a whole do not strongly support fitting for the evolution, we do observe that the free-evolution model appears to provide the best description of the more distant clusters. This is most clearly seen in the T, z plane plotted in Fig. 10, which compares the distribution of the observed clusters in this plane with distributions of large populations simulated from the best-fitting models for each evolutionary scenario. The filled contours show the distribution of simulated clusters from the free-evolution model; these are the same as those shown with the contours in Fig. 6 (middle plot), but with fewer contour levels for clarity. The black solid and red dashed contours show the distributions of clusters simulated from the strong and weak self-similar evolution models, respectively. In all cases the contour levels enclose 90%, 50%, and 10% of the density of simulated clusters.

Figure 10 suggests that while the overall modelling of the XXL-100-GC data do not strongly support fitting for the evolution of the LT relation, the fixed evolution models are not successful at reproducing the observed population of $z > 0.6$ clusters. These clusters appear to prefer stronger than (weak) self-similar evolution, in order that they are sufficiently luminous to be included in the XXL-100-GC sample. With this in mind, it is worth considering the interpretation and implications of a stronger-than-self-similar evolution in the LT relation.

5.5. Interpreting γ_{LT}

The evolution of the LT relation is best expressed as a combination of the evolution and slopes of the LM and MT relations (e.g. Maughan 2014),

$$\gamma_{LT} = \gamma_{LM} - \frac{B_{LM}}{B_{TM}}\gamma_{TM}, \qquad (15)$$

where B_{LM} and γ_{LM} are the slope and power of the evolution term of the LM relation, respectively. We note that B_{TM} is the reciprocal of the slope of the MT relation, B_{MT}.

Thus, stronger-than-self-similar evolution in the LT relation implies stronger-than-self-similar evolution in the LM relation, or weaker-than-self-similar evolution in the TM relation. Stronger-than-self-similar evolution in the LM relation requires either that the baryon fraction within a fixed overdensity be higher at high-z (disfavoured by simulations, e.g. Planelles et al. 2013; Battaglia et al. 2013) or that it be driven by higher density regions of ICM at high-z. In the absence of cool cores, such regions could perhaps be associated with the larger degree of substructure typically seen in higher redshift clusters as we approach the epoch of cluster assembly (e.g. Jeltema et al. 2007; Maughan et al. 2008).

Alternatively, weaker-than-self-similar evolution of the TM relation would require clusters to be cooler for a given mass at high redshift. This could be caused by incomplete virialisation of the ICM at higher redshift. Given that our analysis assumes self-similar evolution of the TM relation, a weaker evolution would mean that we underestimate the mass and hence r_{500} for higher redshift clusters in our Bayesian analysis. This in turn would mean that the luminosity extrapolated to $r_{500,MT}$ would be underestimated and that the core radius (defined via x_{500}) would be underestimated. An underestimation of the core radius for high-z clusters would generally mean that we overestimate the detection probability for those clusters. This would lead us to underestimate the evolution in LT, since fainter clusters would have a higher detection probability than if the core radius were larger. These arguments together imply that any inference of weaker-than-self-similar (i.e. more negative) evolution of the TM relation could be regarded as an upper limit, in the sense that the true evolution could be weaker still.

5.6. Comparisons with simulations

Since we find a positive evolution of the L_{XXL}-T relation, we compare our data to simulations in order to determine what physical processes could be at play that give rise to our observed evolution. Short et al. (2010) studied the evolution of scaling relations using simulations from the Millennium Gas Project (Springel et al. 2005). They employ three different models in their simulations, a gravity-only (GO) control model, a simple preheating model (PC), and a model using feedback from the energy input due to SNe and AGN (FO). Firstly, they show that the local LT relation for the PC and FO runs compare well to the observed LT relation, finding $B_{LT,S10} \approx 3$. Secondly, they find that the evolution of the LT relation behaves differently for the PC and FO simulations. The LT relation evolves negatively for the PC simulation, whereas the FO simulation leads to a positively evolving LT relation. The evolution found using the FO simulation follows the positive evolution of the L_{XXL}-T relation found in this work.

As shown in Sect. 5.5, the interpretation of the evolution of the LT relation is complicated owing to the dependence of the evolution on the LM and TM relations. Short et al. (2010) found

that the evolution of the TM relation evolves negatively, a result implied by the observed positive evolution of the L_{XXL}-T relation. Negative evolution of the TM relation was also found in Pike et al. (2014), using simulations taking into account radiative cooling, star formation, supernovae feedback, and AGN feedback. This provides evidence that the positive evolution observed in the L_{XXL}-T relation is underestimated (see Sect. 5.5). Furthermore, Short et al. (2010) and Pike et al. (2014) find a positively evolving LM relation with a slope steeper than the self-similar expectation. A positively evolving LM relation with a steeper-than-self-similar slope and negatively evolving TM relation (the slope of the TM relation from the simulations agree with the self-similar expectation) would lead to a positively evolving LT relation. Therefore, the evidence of a positively evolving L_{XXL}-T relation (see Sect. 4.5) is in line with the expectation from simulations.

6. Conclusions

We have presented a detailed analysis of the brightest 100 clusters detected in the 50 deg^2 XMM-XXL Survey; the sample spans a wide range of redshift ($0.05 < z < 1.05$), temperature ($0.6 < T < 7.0$ keV), and luminosity ($9 \times 10^{41} < L < 5 \times 10^{43}$ erg s^{-1}). The LT relation has been studied in detail and we present the first measurement of the evolution using a single sample with an internal local baseline LT relation and fully accounting for selection biases. Our main conclusions are as follows.

1. The sample L_{XXL}-T relation has a slope of $B_{LT} = 3.01 \pm 0.27$, not considering the effects of selection biases. This is consistent with previous studies of the observed steep slope of the LT relation when compared to the self-similar expectation.
2. When taking into account the selection effects utilising a Bayesian approach using two forms of the likelihood we find a slope of the soft-band L_{XXL}-T relation of $B_{LT} = 2.63 \pm 0.15$ and a bolometric slope of $B_{LT} = 3.08 \pm 0.15$.
3. After taking into account the selection effects, our data show that the L_{XXL}-T relation prefers an evolution of the form $E(z)^{1.64 \pm 0.77}$. This is consistent with the expected "strong" self-similar evolution; however, is marginally stronger than the "weak" self-similar expectation.
4. Comparisons to clusters detected in the XMM-LSS (a precursor to XXL), which favour a negatively evolving LT relation, can be explained by the different assumptions made for the local baseline LT relation, the assumed mass-temperature relation, and the value of the core radius.
5. Investigating the impact of the assumed mass-temperature relation and the x_{500} parameter, we find that they do not have a significant impact on the L_{XXL}-T relation when using the XXL likelihood model. However, because of the large errors on the evolution, there is a degeneracy between the choice of MT relation, likelihood model, and evolution.
6. We find that small changes in the comparative local baseline LT relation can change the inferred evolution of the L_{XXL}-T relation. This appears to be due to the differing cool core populations in the samples used for the local LT baseline, which are affected by the evolving cool core population and the geometries of the surveys used to draw the cluster samples used for the LT baselines.
7. By comparing our results with those determined from simulations, we find that the positive evolution favours models of cluster formation that include feedback from energy injection from SNe and AGNs.

Our results show that the evolution of the LT relation is strongly affected by the choice of comparative local baseline scaling relations. The XMM-XXL Survey has allowed us for the first time to study in detail the evolution of the LT relation, fully accounting for selection biases, using a single homogeneous sample of clusters. Furthermore, using the data from the ≈ 450 clusters detected in the XXL survey, we will be able to place robust constraints on cosmological parameters.

References

Akritas, M. G., & Bershady, M. A. 1996, ApJ, 470, 706
Allen, S. W., Evrard, A. E., & Mantz, A. B. 2011, ARA&A, 49, 409
Anders, E., & Grevesse, N. 1989, Geochim. Cosmochim. Acta, 53, 197
Andreon, S. 2012, A&A, 546, A6
Andreon, S., & Bergé, J. 2012, A&A, 547, A117
Arnaud, M., Pointecouteau, E., & Pratt, G. W. 2005, A&A, 441, 893
Battaglia, N., Trac, H., Cen, R., & Loeb, A. 2013, ApJ, 776, 81
Bharadwaj, V., Reiprich, T. H., Lovisari, L., & Eckmiller, H. J. 2015, A&A, 573, A75
Böhringer, H., Schuecker, P., Guzzo, L., et al. 2001, A&A, 369, 826
Böhringer, H., Schuecker, P., Pratt, G. W., et al. 2007, A&A, 469, 363
Böhringer, H., Chon, G., Collins, C. A., et al. 2013, A&A, 555, A30
Clerc, N., Sadibekova, T., Pierre, M., et al. 2012, MNRAS, 423, 3561
Clerc, N., Adami, C., Lieu, M., et al. 2014, MNRAS, 444, 2723
Connor, T., Donahue, M., Sun, M., et al. 2014, ApJ, 794, 48
Eckmiller, H. J., Hudson, D. S., & Reiprich, T. H. 2011, A&A, 535, A105
Erben, T., Hildebrandt, H., Miller, L., et al. 2013, MNRAS, 433, 2545
Ettori, S., Tozzi, P., Borgani, S., & Rosati, P. 2004, A&A, 417, 13
Heymans, C., Van Waerbeke, L., Miller, L., et al. 2012, MNRAS, 427, 146
Hilton, M., Romer, A. K., Kay, S. T., et al. 2012, MNRAS, 424, 2086
Hinshaw, G., Larson, D., Komatsu, E., et al. 2013, ApJS, 208, 19
Hoekstra, H., Herbonnet, R., Muzzin, A., et al. 2015, MNRAS, 449, 685
Hudson, D. S., Mittal, R., Reiprich, T. H., et al. 2010, A&A, 513, A37
Jeltema, T. E., Mulchaey, J. S., Lubin, L. M., & Fassnacht, C. D. 2007, ApJ, 658, 865
Kaiser, N. 1986, MNRAS, 222, 323
Kalberla, P. M. W., Burton, W. B., Hartmann, D., et al. 2005, A&A, 440, 775
Kelly, B. C. 2007, ApJ, 665, 1489
Kettula, K., Finoguenov, A., Massey, R., et al. 2013, ApJ, 778, 74
Kotov, O., & Vikhlinin, A. 2005, ApJ, 633, 781
Liddle, A. R. 2007, MNRAS, 377, L74
Lieu, M., Smith, G. P., Giles, P., et al. 2016, A&A, 592, A4 (XXL Survey, IV)
Lovisari, L., Reiprich, T. H., & Schellenberger, G. 2015, A&A, 573, A118
Mann, A. W., & Ebeling, H. 2012, MNRAS, 420, 2120
Mantz, A., Allen, S. W., Ebeling, H., Rapetti, D., & Drlica-Wagner, A. 2010a, MNRAS, 406, 1773
Mantz, A., Allen, S. W., Rapetti, D., & Ebeling, H. 2010b, MNRAS, 406, 1759
Maughan, B. J. 2007, ApJ, 668, 772
Maughan, B. J. 2014, MNRAS, 437, 1171
Maughan, B. J., Jones, L. R., Ebeling, H., & Scharf, C. 2006, MNRAS, 365, 509
Maughan, B. J., Jones, C., Forman, W., & Van Speybroeck, L. 2008, ApJS, 174, 117
Maughan, B. J., Giles, P. A., Randall, S. W., Jones, C., & Forman, W. R. 2012, MNRAS, 421, 1583
McDonald, M., Benson, B. A., Vikhlinin, A., et al. 2014, ApJ, 794, 67
Meng, X.-L. 1994, The Annals of Statistics, 22, 1142
Osmond, J. P. F., & Ponman, T. J. 2004, MNRAS, 350, 1511
Pacaud, F., Pierre, M., Refregier, A., et al. 2006, MNRAS, 372, 578
Pacaud, F., Pierre, M., Adami, C., et al. 2007, MNRAS, 382, 1289
Pacaud, F., Clerc, N., Clerc, Giles, P. A., et al. 2016, A&A, 592, A2 (XXL Survey, II)
Pierre, M., Pacaud, F., Adami, C., et al. 2016, A&A, 592, A1 (XXL Survey, I)

Pike, S. R., Kay, S. T., Newton, R. D. A., Thomas, P. A., & Jenkins, A. 2014, MNRAS, 445, 1774

Planelles, S., Borgani, S., Dolag, K., et al. 2013, MNRAS, 431, 1487

Pratt, G. W., & Arnaud, M. 2002, A&A, 394, 375

Pratt, G. W., Croston, J. H., Arnaud, M., & Böhringer, H. 2009, A&A, 498, 361

Press, W. H., Flannery, B. P., & Teukolsky, S. A. 1986, Numerical recipes. The art of scientific computing

R Core Team 2014, R: A Language and Environment for Statistical Computing, R Foundation for Statistical Computing, Vienna, Austria

Reichert, A., Böhringer, H., Fassbender, R., & Mühlegger, M. 2011, A&A, 535, A4

Romer, A. K., Viana, P. T. P., Liddle, A. R., & Mann, R. G. 2001, ApJ, 547, 594

Santos, J. S., Tozzi, P., & Rosati, P. 2011, Mem. Soc. Astron. It. Supp., 17, 66

Short, C. J., Thomas, P. A., Young, O. E., et al. 2010, MNRAS, 408, 2213

Smith, R. K., Brickhouse, N. S., Liedahl, D. A., & Raymond, J. C. 2001, ApJ, 556, L91

Spiegelhalter, D. J., Best, N. G., Carlin, B. P., & Van Der Linde, A. 2002, J. Roy. Stat. Soci.: Ser. B, 64, 583

Springel, V., White, S. D. M., Jenkins, A., et al. 2005, Nature, 435, 629

Stanek, R., Evrard, A. E., Böhringer, H., Schuecker, P., & Nord, B. 2006, ApJ, 648, 956

Sun, M., Voit, G. M., Donahue, M., et al. 2009, ApJ, 693, 1142

Takey, A., Schwope, A., & Lamer, G. 2013, A&A, 558, A75

Tinker, J., Kravtsov, A. V., Klypin, A., et al. 2008, ApJ, 688, 709

Vikhlinin, A., van Speybroeck, L., Markevitch, M., Forman, W. R., & Grego, L. 2002, ApJ, 578, L107

Vikhlinin, A., Burenin, R., Forman, W. R., et al. 2007, in Heating versus Cooling in Galaxies and Clusters of Galaxies, eds. H. Böhringer, G. W. Pratt, A. Finoguenov, & P. Schuecker, 48

Vikhlinin, A., Burenin, R. A., Ebeling, H., et al. 2009, ApJ, 692, 1033

Willis, J. P., Pacaud, F., Valtchanov, I., et al. 2005, MNRAS, 363, 675